1991

Ionic structure of methane flames

Timothy Wayne Pedersen
Iowa State University

Order Number 9202384

Ionic structure of methane flames

Pedersen, Timothy Wayne, Ph.D.

Iowa State University, 1991

U·M·I
300 N. Zeeb Rd.
Ann Arbor, MI 48106

Ionic structure of methane flames

by

Timothy Wayne Pedersen

A Dissertation Submitted to the

Graduate Faculty in Partial Fulfillment of the

Requirements for the Degree of

DOCTOR OF PHILOSOPHY

Major: Mechanical Engineering

Approved:

Signature was redacted for privacy.

In Charge of Major Work

Signature was redacted for privacy.

For the Major Department

Signature was redacted for privacy.

For the Graduate College

Iowa State University
Ames, Iowa
1991

TABLE OF CONTENTS

LIST OF TABLES

LIST OF FIGURES

ACKNOWLEDGEMENTS

I would like to thank my program of study committee, Dr. James Hill, Dr. Joseph Prusa, Dr. Howard Shapiro, and Dr. Jerald Vogel for the valuable time they spent in preparing for my written and oral exams.

I feel fortunate to have had Dr. Robert Brown as my major professor. Dr. Brown's positive outlook on difficulties and his patience during the slow times was always appreciated. He was there with encouragement and understanding when I was forced to face some tough personal battles during my years of research. He also has an unique insight to problem solving that I hope to possess at some point in my career. It is therefore, with deep gratitude that I thank Dr. Brown for his careful guidance of my research.

Lastly, I would like to express my appreciation to my family. To my parents, Jean Pedersen and the late Lindstrom "Pete" Pedersen Jr. who instilled in me the desire to set high goals and, more importantly, the discipline, ambition, and determination to succeed. To my older brother, Lindy, I thank you for the example you set with your attitude that hard work will always pay off. Your a great guy and a wonderful brother to whom I look up to. Debi, you were just fourteen when I started my college career and now you are a married woman. You sent me some encouraging letters my first year in college and in tough times I would recall the contents of those letters for

support. Thank you for being a wonderful sister. To my wife, Lisa, I give my greatest appreciation. You have to be the most unselfish and loving woman any man could ever hope to have as a wife. You have sacrificed many comforts and have tolerated graduate school with patience and good humor. When times were rough, I could always count on you for a supportive comment and smile. Lisa, thank you and I love you!

NOMENCLATURE

A – area

B – stretching parameter

C_p – specific heat at constant pressure

D – diffusion coefficient

E – electric field

e – electron charge

E_a – activation energy

E_e – effective activation energy

G – Gibb's free energy

H – mass specific enthalpy

h – molar specific enthalpy

J_i – mass flux

j_s – saturation current flux

K – equilibrium constant

k – rate coefficient

L – domain length

M – molecular weight

N – number of nodes

n – number density

P – products of the reaction

R – universal gas constant, reactants of the reaction

T – temperature

t – time

u – velocity

V – voltage

X – mole fraction

x – spatial variable

Y – mass fraction

Γ – generic variable

ϵ_o – permissivity constant

λ – thermal conductivity

Φ – equivalence ratio

ρ – density

μ – mobility

φ – generic variable

ψ – transposed spatial variable

ω – mass production rate per unit volume

subscripts

a	–	ambipolar
e	–	electron
eq	–	equilibrium
f	–	final, forward
H	–	heat flux
i	–	node or species designation
j	–	species designation
m	–	multicomponent
N	–	number of nodes
nspc	–	number of species
o	–	initial value
r	–	reverse
T	–	thermal
$+(-)$	–	positive (negative) charge

superscripts

c	–	cold
h	–	hot

1. INTRODUCTION

The objective of this research is to predict the ionic structure of methane flames. An understanding of the process involved in the ionization of flames could lead to electrical control of blow-off limits, flame speed, and formation of soot.

The numerical simulation of flames requires detailed reaction mechanisms. Over the past few years several researchers [1, 2, 3, 4, 5, 6, 7] have proposed reaction mechanisms that accurately describe methane combustion phenomena. However, none of these mechanisms include ionic species. It is thought that the inclusion of ions in the model would unduly complicate it since ion concentrations are small compared to the neutral species concentrations. Since the focus of this research is to investigate the ionic structure of methane flames, reactions involving ionic species must be included in the reaction mechanism.

The neutral species reaction mechanism used in this work is a methane mechanism proposed by Coffee [2]. It includes reactions for the simulation of hydrogen flames. This makes it possible to investigate the behavior of ions in hydrogen/methane flames also.

The ionic reaction mechanism is a group of reactions that includes ionic species. This mechanism includes the chemiionization reactions

$$CH + O \rightarrow CHO^+ + e^-$$

and

$$CH^* + O \rightarrow CHO^+ + e^-.$$

Ion–molecule, proton transfer, and dissociation recombination reactions are also part of the ionic species mechanism. This mechanism was added to the neutral species reaction mechanism to form a comprehensive reaction mechanism describing methane combustion.

Lawton and Weinberg [8] have shown that by placing an ion–producing flame in an electric field, the saturation current for that flame can be measured. In general, ions are removed from a flame by recombination with electrons. When the flame is immersed in an electric field, ions are removed by recombination as well as by the electric field. The positive ions are attracted to the cathode. The negative charge, 99% of which is carried by free electrons [9], is attracted to the anode. As the potential is increased, removal of the ions due to the electric field becomes dominant over removal by recombination. Eventually the electric field will remove the ions from the flames as fast as they are produced by chemiionization. The current produced by the movement of these ions when this phenomena occurs is called the saturation current, j_s. It is defined as the rate of ion removal from the flame per unit area of flame front.

Lawton and Weinberg [8] have shown that by plotting $\ln(j_s)$ vs. $1/T_f$ results in straight lines. The slope of these lines are equivalent to an effective activation energy. It is thought that these activation energies are characteristic of the reaction or reactions responsible for the production of ions in flames.

Lawton and Weinberg [8] and Peeter and Van Tiggelen [10] have measured the saturation currents and subsequent effective activation energies for methane flames.

However, these values were not related to a detailed reaction mechanism.

To computationally simulate these experiments requires advanced solution techniques. This research uses the split-operator technique [11] along with TRANSEQI [12] to solve the species conservation equations describing a one-dimensional, premixed, laminar flame. To simulate the electric field that is imposed on the flame, Poisson's equation is solved. This approach provides a means for calculating the saturation current produced by the flame. Experimental temperature profiles are used instead of solving the energy equation, thereby automatically accounting for heat losses due to radiation, convection, and conduction. It also makes the solution process easier in terms of shorter computation times.

Simply by changing the final flame temperature of the experimental profile, the variation of the saturation current as a function of final flame temperature can be determined. The effective activation energies for a lean, stoichiometric, and rich flame are calculated in this work. The results are then related to reactions in the ionic reaction mechanism. The final step is to predict the ionic structure of methane flames.

2. BACKGROUND

One of the earliest observations of charged species in hydrocarbon flames dates back to 1801 when Volta [13] showed that the static charge on a nonconductor was dissipated when the material was introduced into the flame. A short time later in 1802, Erman [14] found that by inserting wires into different parts of a flame a current was produced.

This led to researchers trying to measure flame conductivity. Electric fields controlling flame deflection was another area of intense research. However, most of the research conducted in these early years was poorly documented. Missing was information about flame equivalence ratios, flow rates, and burner dimensions. One important result did come of this research. It showed ion concentrations in flames could exceed 10^{11} ions/cm^3.

It was Arrhenius [15] in 1891 who proposed that the negative charge carrier in the flame was free electrons. He based his conclusion on results obtained through mobility measurements. In 1965 Calcote [9] used electric probes and a mass spectrometer to show that 99% of the negative charge was indeed carried by free electrons.

In 1910 Thompson [16] suggested that electrons play an important role in flame propagation. Since the electrons are much smaller than positive ions, it was thought that they diffused quickly into the unburned gases. Therefore, electrons initiated or

assisted in the initiation of reactions that produced free radicals. Tanford and Pease [17] in 1947 proposed a similar theory for H atoms. Because the H atom is also very small, it too was thought to diffuse upstream and participate in initiation reactions.

Up until 1947, it was thought that ions in flames were produced by thermal ionization. It was Calcote [18] who first disproved the general belief that ionization in flames was thermal in origin. In his review of ions in flames, he showed sufficient data existed in literature to support his theory that ions in flames were formed by a different mechanism. He proposed a kinetic mechanism as opposed to an equilibrium mechanism as being responsible for the formation of ionic species. This mechanism responsible for the formation of ions in flames was termed chemiionization.

This concept of chemiionization was readily accepted by most flame researchers but it was not until the 1950s that flame ionization research really began. The laboratories of Sugden, Van Tiggelen, and Calcote were the first to build flame ion mass spectrometers and begin intense research into ion processes in flames.

Littlewood [19] in 1962 and Sugden [20] in 1965 were two of the first researchers who focused on the reaction or reactions responsible for chemiionization.

In 1960, Desty *et al.* [21] showed that no ionization occurred in H_2/O_2 or $H_2/O_2/N_2$ flames. Any ions observed were attributed to impurities in the fuel gases. This absence of ions in hydrogen flames allowed for the determination of hydrocarbon using gas chromatographic flame ionization detectors. These instruments were able to detect trace amounts of hydrocarbon by measuring the flame conductivity. This allowed Littlewood [19] to show that the reactions responsible for ion formation must involve species that contain both carbon and hydrogen.

Bulewicz and Padley [22] in 1963 showed that the number of ions produced per

C atom was constant for any homologous series of fuels. Through this research it was concluded that CO and CO_2 yielded no chemiions. It was apparent that to produce the full quota of ionization, the carbon atom must be bonded to hydrogen atoms or to hydrogen atoms and other carbon atoms. Bulewicz and Padley [22] then showed that one of the reactants in the elementary process producing chemiions contained a single carbon and hydrogen atom. It was thought that CH was this reactant.

The presence of hydrocarbons in flames is a necessary but not sufficient condition for ionization in flames. It had also been proposed that oxygen containing species must also be present for ionization to occur in flames. Calcote [23] substantiated this claim with experimental data that showed maximum ion concentrations occurred at or near stoichiometric conditions for several hydrocarbon flames. Bulewicz and Padley [22] demonstrated that the oxygen-containing species that participates in the elementary ionization reaction with CH could not be H_2O, OH, CO, CO_2, or O_2. Through additional tests, it was concluded that the O atom must be the one responsible for ionization. Fontijn *et al.* [24, 25] provided additional evidence for the dominant role played by O in the ion formation.

Up to this point, it appeared that CH and O were the reactants in the bimolecular reaction that were responsible for ionization. This implied that CHO^+ must be the first ion formed. Therefore,

$$CH + O \rightarrow CHO^+ + e^-$$

was the reaction responsible for the ion concentration in flames.

Research in 1965 and 1967 [26, 27, 28] showed that electronically excited CH was not present in large enough quantities to be responsible for ionization in flames. This research was performed on lean to slightly rich hydrocarbon flames. Cool and Tjossem

[29] showed that the high rate of reaction of electrically excited CH made it a possible source of CHO^+. More recently, research by Eraslan and Brown [30] has shown that electronically excited CH was responsible for ion formation in rich acetylene flames with equivalence ratios between 1.7 and 2.5. The mechanism generally accepted as being responsible for ionization in flames consists of

$$CH + O \rightarrow CHO^+ + e^-$$

and

$$CH^* + O \rightarrow CHO^+ + e^-.$$

The latter of the two reactions being important only in rich flames [30].

The rate at which the ground state CH reaction proceeds was determined by Warnatz [7] in 1984. Cool and Tjossem [29] determined that the reaction of electrically excited CH with oxygen atoms to be 2000 times faster than the same reaction with ground state CH.

Information pertaining to the identities of ions in flames has been obtained directly from the flame using a mass spectrometer. Numerous ions, including CHO^+, have been identified by researchers as being present in hydrocarbon flames. Green and Sugden [31] were the first to divide the ions into three categories: true flame ions, ions formed in the mass spectrometer, and ions of unknown origin. In doing so, the list of major true flame ions present in all hydrocarbon flames was reduced to only four: CHO^+, H_3O^+, $C_3H_3^+$, and CH_3^+. This list was increased by one species when $C_2H_3O^+$ was found to be the dominant ion in lean acetylene flames [30, 32].

The concentration of CHO^+ found in hydrocarbon flames has been small. It was concluded that CHO^+ must therefore take part in a rapid ion–molecule reaction to

produce other observed species. Just downstream of the reaction zone large quantities of H_2O were reported along with a dominant ionic species, H_3O^+. The reaction thought to be responsible for the production of this ion and consumption of CHO^+ was [33]

$$CHO^+ + H_2O \rightarrow CO + H_3O^+.$$

For equivalence ratios close to unity, H_3O^+ was found to be the dominant ion [9, 23, 32].

The dominant ion in lean acetylene flames is $C_2H_3O^+$. It was thought to be created by the proton transfer reaction [9, 32]

$$H_3O^+ + CH_2CO \rightarrow C_2H_3O^+ + CO + H_2.$$

However, this reaction was shown to be inadequate for the production of $C_2H_3O^+$. It did not correctly predict the profile of the $C_2H_3O^+$ ion [34]. The alternate reaction

$$H_3O^+ + C_2H_2 \rightarrow C_2H_3O^+ + H_2$$

was proposed by Brown and Eraslan [30] as the source of this ion. Goodings *et al.* [35] experimentally showed H_3O^+ to be the dominant ion in lean methane flames. The source of this ion was thought to be from the proton transfer reaction

$$CHO^+ + H_2O \rightarrow CO + H_3O^+.$$

As the flame is made rich, $C_3H_3^+$ becomes the dominant ion [23, 32]. The source of this ion was thought to be

$$CH_3^+ + C_2H_2 \rightarrow C_3H_3^+ + H_2$$

and

$$H_3O^+ + C_3H_2 \rightarrow C_3H_3^+ + H_2O.$$

In research performed by Brown and Eraslan [30], a sensitivity analysis showed

$$CH_3^+ + C_2H_2 \rightarrow C_3H_3^+ + H_2$$

to play the major role of producing the $C_3H_3^+$ ion.

Diffusion and recombination are two processes by which the concentration of these ions can be reduced. A large ratio of electron concentration to negative ion concentration has been found in hydrocarbon flames. The electron, with its small mass and high mobility, has a high diffusion rate out of the flame. The result is a net positive charge in the flame. The positive ions diffusion rate increases because of this net charge effect. The self-induced electric field increases in magnitude up to a point where the motion of the electrons is so retarded that both the electrons and positive ions diffuse at the same rate. This process is called ambipolar diffusion. Ambipolar diffusion has been shown to be important in low pressure flames only.

Three-body, radiative, dissociative, and mutual neutralization are four mechanisms by which electrons can recombine. Calcote [23] has reported the recombination rate for ions to be independent of pressure. Recombination by three-body recombination was eliminated since it is pressure dependent and unimportant in flames at pressures lower than 760 torr. Because of the absence of detectable continuum emissions in flames, Calcote [23] has dismissed radiative recombination of electrons. Mutual neutralization was also dismissed as a possible recombination path since its products are never observed in flames. The only other proposed mechanism remaining for electron consumption was dissociative recombination. Two possible dissociative

recombination reactions [33] were

$$H_3O^+ + e^- \rightarrow H_2O + H$$

and

$$H_3O^+ + e^- \rightarrow H + H + OH.$$

Lawton and Weinberg in 1969 [36] suggested that

$$H_3O^+ + e^- \rightarrow H_2O + H$$

was responsible for recombination since it is highly exothermic. This reinforces the idea that the deactivation of H_3O^+ was due to dissociation recombination. An idea that is based on the experimental observation that H_3O^+ is the dominant ion in the recombination zone of flames.

When the electric field is applied to the flame a current is produced by the movement of ions. The ions are being removed from the flame by recombination and electric field effects. As the field intensity is increased, the ion current increases at the expense of recombination. Further increase in the potential causes an increase in ion current to a point where the ion current becomes constant. At this point, ions are being removed by the electric field at the same rate in which they are generated. This maximum current is called the saturation current and is denoted by j_s. It is equal to the rate of generation of charge per unit area of flame front.

By measuring the saturation current, the ion generation rates can be determined. It was shown by Lawton and Weinberg [8] that the saturation current can be used to determine effective activation energies for ion-generating reactions. This was done by measuring the variation of saturation current with flame temperature. Therefore,

the saturation current became an important and easily measured tool in the study of flame ionization.

In their experiments Lawton and Weinberg [8] used a porous disc burner as the cathode. The anode was a plane electrode mounted parallel to the flame and at a small distance above it. One advantage to the system was that the flame is always flat and by varying the flow rate, the saturation current was measured as a function of flame temperature. The ability to change the flow rate allowed for control over the heat loss and final flame temperature without altering the flame composition. The currents were measured using a microammeter. The researchers carried out experiments on methane, ethylene, and propane/air mixtures. They also investigated hydrogen/air mixtures to which trace amounts of hydrocarbon were added.

Saturation currents as a function of final flame temperature were not documented by Lawton and Weinberg [8] for hydrocarbon flames. However, the saturation current as a function of equivalence ratio for each hydrocarbon flame was documented.

For the hydrocarbon seeded hydrogen/air flame, the variation of saturation currents with final flame temperature was recorded. The hydrogen/air flames were seeded with up to 1% hydrocarbon.

Lawton and Weinberg [8] showed that the slope of $\ln(j_s)$ vs. $1/T_f$ was the effective activation energy for the ionization process. Effective activation energies reported for the investigated flames ranged in value from 37.5 ± 2 kcal/mole to 67 ± 4 kcal/mole depending on equivalence ratios and hydrocarbon fuel. The researchers recognized that the effective activation energies were much larger than the activation energies for proposed chemiionization processes in flames. They did not draw any firm conclusions about the resulting values of effective activation energies. It was

emphasized by the researchers that the work presented was purely to establish a practical method for the study of ion generation rates in flames.

In 1968 Peeters and Van Tiggelen [10] measured the rate of the chemiionization process for flames with equivalence ratios close to unity. Their experimental set-up included included a Powling–Egerton type burner open to the atmosphere. The burner served as the cathode and a conducting plate placed above the flame served as the anode. They measured the saturation current for various flame temperatures. The effective activation energy was found to be 73 kcal/mole. However, no attempt was made to relate this activation energy to a detailed reaction mechanism.

About a decade later, Bertrand *et al.* [37] measured the burning velocity of a stoichiometric methane flame stabilized on a flat flame burner. The researchers measured the variation of saturation current with final flame temperature. The effective activation energy for this flame was equal to 53 kcal/mole. Again, no attempt was made to relate the effective activation energy to a reaction mechanism.

Numerical methods used in flame simulations have progressed to the point where it is now computationally possible to predict the saturation currents in flames. The effective activation energies can then be determined which makes it possible to predict the ionic structure of flames.

The focus of this research was to relate the effective activation energies obtained from the saturation currents to a reaction mechanism. The ionic structure of a methane flame was investigated for equivalence ratios ranging from 0.2 to 2.13. The saturation currents for these flames were predicted for various final flame temperature which led to an effective activation energy. The reaction that was responsible for these effective activation energies was then determined through a sensitivity analysis.

The computer model allowed the ion movement to be traced through the reaction mechanism.

3. CHEMICAL KINETICS

It is essential to establish a comprehensive chemical kinetic mechanism prior to studying combustion phenomena in premixed flames. The mechanism must include reactions necessary to simulate a methane flame. Part of this research will be conducted on ion production in hydrogen flames seeded with methane. Therefore, the mechanism must also include reactions necessary to simulate a hydrogen flame. Such a mechanism must include reactions for the oxidation of fuel for both flames. The ionic mechanism must allow for the production and depletion of ions through chemiionization, ion–molecule reactions, and dissociative recombination. The ionic mechanism was developed with the knowledge that ions do not form in hydrogen flames. Only major ions are considered in the ionic mechanism since they constitute more than 85% of the total ion current. The entire mechanism is listed in Table 3.1.

3.1 Neutral Species Mechanism

A number of researchers have performed detailed studies of the chemical kinetics of methane flames [1, 2, 3, 4, 5, 6, 7]. The reactions that make up the neutral species mechanism were taken from several authors and assembled by Coffee [2]. Reactions for the formation of $CH^*(A^2\Delta)$ and CH are taken from an acetylene flame mechanism that was assembled from other authors by Eraslan and Brown [30].

The first 21 reactions were taken from Dixon-Lewis [38]. These were verified in studies performed on $H_2/O_2/N_2$ and $CO/H_2/O_2/N_2$ flames [39]. The inclusion of these reactions make it possible to study the consequences of seeding hydrogen flames with methane.

Dean *et al.* [40, 41] performed a series of shock tube experiments. These experiments led to the inclusion of reactions 22–29. The first four reactions of this set allow for the formation of CH_3 from CH_4. Formaldehyde (CH_2O) is then formed from CH_3.

The reactions that include CHO (rxns. 30-33) have reaction rates that are not well known. The values from Dixon-Lewis [38] are used for the lack of better data.

Reactions 34–37 include the oxidation of CH_4. This set of reactions were shown by Gelinas [42] to be necessary for modeling a CH_4 flame.

The primary source of C_2 hydrocarbons is through reaction 38. The rate for this reaction was taken from Warnatz [6] and Dixon-Lewis [38] which was then modified for atmospheric conditions by Luther and Troe [43]. Reactions 38–56 make up the road map followed by C_2H_6 to the formation of CH_3 and CO:

$$C_2H_6 \rightarrow C_2H_5 \rightarrow C_2H_4 \rightarrow C_2H_3 \rightarrow C_2H_2 \rightarrow CH_3, CO.$$

Also, reactions 46 and 47 form a pathway for the production of CH_2O.

The kinetics describing CH_2 chemistry is provided in reactions 57–62 [42]. These reactions were first used in the modeling of CH_4/air flames by Coffee [2].

Work performed in the area of ionic mechanisms for methane flames is very limited. Therefore, it was necessary to expand the neutral species mechanism to include reactions that form precursors vital to ionization. Since chemiionization is believed to be the major source of ions in hydrocarbon flames, reactions that form the precursors CH and $CH^*(A^2\Delta)$ which in turn feed the chemiionization reactions

are included in the mechanism. These reactions (rxns. 63-73) were taken from a mechanism proposed by Eraslan and Brown [30] for acetylene flames and added to the neutral species mechanism.

Table 3.1: Neutral species reaction mechanism (Reaction rates are in cm^3-mole-sec-cal units, $k = AT^B e^{\frac{-E_a}{RT}}$.)

	Reaction	A	B	E_a
1	$OH + H_2 \rightleftharpoons H_2O + H$	1.17E+09	1.3000	1825.0
2	$H + O_2 \rightleftharpoons OH + O$	1.42E+14	0.0000	8250.0
3	$O + H_2 \rightleftharpoons OH + H$	1.80E+10	1.0000	4480.0
4	$H + O_2 + M' \rightleftharpoons HO_2 + M'$	1.03E+18	-0.7200	0.0
5	$H + HO_2 \rightleftharpoons OH + OH$	1.40E+14	0.0000	540.0
6	$H + HO_2 \rightleftharpoons O + H_2O$	1.00E+13	0.0000	540.0
7	$HO_2 + H \rightleftharpoons O_2 + H_2$	1.25E+13	0.0000	0.0
8	$HO_2 + OH \rightleftharpoons O_2 + H_2O$	7.50E+12	0.0000	0.0
9	$HO_2 + O \rightleftharpoons O_2 + OH$	1.40E+13	0.0000	540.0
10	$H + H + H_2 \rightleftharpoons H_2 + H_2$	9.20E+16	-0.6000	0.0
11	$H + H + O_2 \rightleftharpoons H_2 + O_2$	1.00D+18	-1.0000	0.0
12	$H + H + H_2O \rightleftharpoons H_2 + H_2O$	6.00E+19	-1.2500	0.0
13	$H + H + CO \rightleftharpoons H_2 + CO$	1.00E+18	-1.0000	0.0
14	$H + H + CO_2 \rightleftharpoons H_2 + CO_2$	5.49E+20	-2.0000	0.0
15	$H + H + CH_4 \rightleftharpoons H_2 + CH_4$	5.49E+20	-2.0000	0.0
16	$H + OH + M'' \rightleftharpoons H_2O + M''$	1.60E+22	-2.0000	0.0
17	$H + O + M'' \rightleftharpoons OH + M''$	6.20E+16	-0.6000	0.0
18	$OH + OH \rightleftharpoons H_2O + O$	5.72E+12	0.0000	390.0
19	$OH + CO \rightleftharpoons CO_2 + H$	1.57E+07	1.3000	-385.0
20	$O + CO + M' \rightleftharpoons CO_2 + M'$	5.40E+15	0.0000	2300.0
21	$H + CO + M' \rightleftharpoons CHO + M'$	5.00E+14	0.0000	755.0
22	$CH_4 + O \rightleftharpoons CH_3 + OH$	4.07E+14	0.0000	7040.0
23	$CH_4 + H \rightleftharpoons CH_3 + H_2$	7.24E+14	0.0000	7590.0
24	$CH_4 + OH \rightleftharpoons CH_3 + H_2O$	1.55E+06	2.1300	1230.0
25	$CH_4 + M \rightleftharpoons CH_3 + H + M$	4.68E+17	0.0000	46910.0
26	$CH_3 + O \rightleftharpoons CH_2O + H$	6.02E+13	0.0000	0.0
27	$CH_2O + O \rightleftharpoons CHO + OH$	1.82E+13	0.0000	1550.0
28	$CH_2O + H \rightleftharpoons CHO + H_2$	3.31E+14	0.0000	5290.0
29	$CH_2O + OH \rightleftharpoons CHO + H_2O$	7.58E+12	0.0000	72.0
30	$CHO + O_2 \rightleftharpoons CO + HO_2$	3.00E+12	0.0000	0.0

Table 3.1 (Continued)

	Reaction	A	B	E_a
31	$CHO + H \rightleftharpoons CO + H_2$	4.00E+13	0.0000	0.0
32	$CHO + OH \rightleftharpoons CO + H_2O$	5.00E+12	0.0000	0.0
33	$CHO + O \rightleftharpoons CO + OH$	1.00E+13	0.0000	0.0
34	$CH_2O + CH_3 \rightleftharpoons CHO + CH_4$	2.23E+13	0.0000	2590.0
35	$CH_3 + OH \rightleftharpoons CH_2O + H_2$	3.98E+12	0.0000	0.0
36	$CH_3 + HO_2 \rightleftharpoons CH_4 + O_2$	1.02E+12	0.0000	200.0
37	$CO + HO_2 \rightleftharpoons CO_2 + OH$	1.50E+14	0.0000	11900.0
38	$CH_3 + CH_3 \rightleftharpoons C_2H_6$	4.56E+17	-7.6500	4250.0
39	$C_2H_6 + O \rightleftharpoons C_2H_5 + OH$	2.51E+13	0.0000	3200.0
40	$C_2H_6 + H \rightleftharpoons C_2H_5 + H_2$	5.00E+02	3.5000	2620.0
41	$C_2H_6 + OH \rightleftharpoons C_2H_5 + H_2O$	6.63E+13	0.0000	675.0
42	$C_2H_5 + H \rightleftharpoons C_2H_6$	7.23E+13	0.0000	0.0
43	$C_2H_5 + H \rightleftharpoons CH_3 + CH_3$	3.73E+13	0.0000	0.0
44	$C_2H_5 \rightleftharpoons C_2H_4 + H$	2.29E+11	0.0000	19120.0
45	$C_2H_5 + O_2 \rightleftharpoons C_2H_4 + HO_2$	1.53E+12	0.0000	2446.0
46	$C_2H_4 + O \rightleftharpoons CH_2 + CH_2O$	2.53E+13	0.0000	2516.0
47	$C_2H_4 + OH \rightleftharpoons CH_2O + CH_3$	5.00E+13	0.0000	3020.0
48	$C_2H_4 + O \rightleftharpoons C_2H_3 + OH$	2.53E+13	0.0000	2516.0
49	$C_2H_4 + O_2 \rightleftharpoons C_2H_3 + HO_2$	1.33E+15	0.0000	27680.0
50	$C_2H_4 + H \rightleftharpoons C_2H_3 + H_2$	2.00E+15	0.0000	10000.0
51	$C_2H_4 + OH \rightleftharpoons C_2H_3 + H_2O$	4.40E+14	0.0000	3270.0
52	$C_2H_3 + M \rightleftharpoons C_2H_2 + H + M$	3.01E+16	0.0000	20380.0
53	$C_2H_3 + O_2 \rightleftharpoons C_2H_2 + HO_2$	1.57E+13	0.0000	5030.0
54	$C_2H_3 + H \rightleftharpoons C_2H_2 + H_2$	7.53E+13	0.0000	0.0
55	$C_2H_3 + OH \rightleftharpoons C_2H_2 + H_2O$	1.00E+13	0.0000	0.0
56	$C_2H_2 + OH \rightleftharpoons CH_3 + CO$	5.48E+13	0.0000	6890.0
57	$CH_3 + H \rightleftharpoons CH_2 + H_2$	2.00E+11	0.7000	-1500.0
58	$CH_3 + OH \rightleftharpoons CH_2 + H_2O$	6.00E+10	0.7000	1010.0
59	$CH_2 + O_2 \rightleftharpoons CHO + OH$	1.00E+14	0.0000	1860.0
60	$CH_2 + O_2 \rightleftharpoons CH_2O + O$	1.00E+14	0.0000	1860.0

Table 3.1 (Continued)

	Reaction	A	B	E_a
61	$CH_2 + O_2 \rightleftharpoons CO_2 + H_2$	1.00E+14	0.0000	1860.0
62	$CH_2 + H \rightleftharpoons CH + H_2$	4.00E+13	0.0000	0.0
63	$CH + O \rightleftharpoons CO + H$	4.00E+13	0.0000	0.0
64	$CH + O_2 \rightleftharpoons CO + OH$	2.00E+13	0.0000	0.0
65	$C_2H + O \rightleftharpoons CO + CH$	1.00E+13	0.0000	0.0
66	$CH^* + M \rightleftharpoons CH + M$	4.00E+10	0.5000	0.0
67	$CH^* + O_2 \rightleftharpoons CH + O_2$	2.40E+12	0.5000	0.0
68	$CH^* \rightleftharpoons CH$	1.90E+06	0.0000	0.0
69	$C_2H + O_2 \rightleftharpoons CH^* + CO_2$	4.50E+15	0.0000	25000.0
70	$C_2H + O \rightleftharpoons CH^* + CO$	7.10E+11	0.0000	0.0
71	$C_2H_2 + H \rightleftharpoons C_2H + H_2$	6.00E+13	0.0000	23651.0
72	$C_2H_2 + OH \rightleftharpoons C_2H + H_2O$	1.00E+13	0.0000	7000.0
73	$C_2H + O_2 \rightleftharpoons CO + CHO$	5.00E+13	0.0000	1505.0
74	$CH + O \rightleftharpoons CHO^+ + e^-$	2.52E+11	0.0000	1700.0
75	$CH^* + O \rightleftharpoons CHO^+ + e^-$	5.01E+11	0.0000	1700.0
76	$CHO^+ + H_2O \rightleftharpoons H_3O^+ + CO$	1.00E+16	-0.0897	0.0
77	$H_3O^+ + C_2H_2 \rightleftharpoons C_2H_3O^+ + H_2$	8.39E+15	0.0000	0.0
78	$CHO^+ + CH_2 \rightleftharpoons CH_3^+ + CO$	5.62E+14	-0.0060	0.0
79	$H_3O^+ + CH_2 \rightleftharpoons CH_3^+ + H_2O$	6.17E+14	-0.0060	0.0
80	$CH_3^+ + C_2H_2 \rightleftharpoons C_3H_3^+ + H_2$	7.24E+14	0.0000	0.0
81	$C_3H_3^+ + H_2O \rightleftharpoons C_2H_3O^+ + CH_2$	7.24E+14	0.0000	0.0
82	$CH_3^+ + CO_2 \rightleftharpoons C_2H_3O^+ + O$	7.24E+14	0.0000	0.0
83	$H_3O^+ + e^- \rightleftharpoons H_2O + H$	2.29E+18	-0.5000	0.0
84	$C_3H_3^+ + e^- \rightleftharpoons$ products	1.50E+19	-0.5000	0.0
85	$CH_3^+ + e^- \rightleftharpoons CH_2 + H$	2.29E+18	-0.5000	0.0
86	$C_2H_3O^+ + e^- \rightleftharpoons M + H$	2.29E+18	-0.5000	0.0

3.2 Ionic Species Mechanism

The ionic mechanism consists of reactions 74–86. It was developed with the intention of simulating the major ions present in methane flames.

From the time when ions were first detected in flames [13, 14] until 1947, it was believed that ions were formed by thermal ionization. Calcote [18] proposed ions were formed by a kinetic mechanism in a process called chemiionization. Between 1947 and the present, many reactions responsible for chemiionization have been proposed and rejected. Currently, it is believed that

$$CH + O \rightarrow CHO^+ + e^-$$

and

$$CH^* + O \rightarrow CHO^+ + e^-$$

are responsible for the chemiionization process [10, 30]. The presence of the CHO^+ ion is the prerequisite for the production of all other ions in the flame. These ions include CH_3^+, $C_2H_3O^+$, $C_3H_3^+$, and H_3O^+. Experiments have shown other ions to be present but are small in concentration compared to the aforementioned ions [36] and are neglected in the present study. Calcote [23] proposed that if chemiionization produced CHO^+, then it would be quickly consumed by H_2O to produce H_3O^+ via

$$CHO^+ + H_2O \rightarrow CO + H_3O^+,$$

thereby making H_3O^+ the dominant ion in lean to rich hydrocarbon flames. He then went further to suggest that the H_3O^+ ion recombined with an electron to produce H_2O via

$$H_3O^+ + e^- \rightarrow H_2O + H.$$

Ay *et al.* [44] proceeded one step further and concluded that these reactions produced ion concentrations in agreement with experimentally measured values. Brown and Eraslan [30] in 1988 proposed that

$$H_3O^+ + C_2H_2 \rightarrow C_2H_3O^+H_2$$

and

$$CH_3^+ + C_2H_2 \rightarrow C_3H_3^+ + H_2$$

were the reactions responsible for the formation of $C_2H_3O^+$ and $C_3H_3^+$. Therefore, these five reactions are included as the driving mechanism behind ion production and recombination in this model.

There are four mechanisms available for the deactivation of ions in flames. Three of these mechanisms include three-body, radiative, and mutual neutralization recombination. These three types of recombination have been ruled out by previous research [23] as unimportant paths for deactivation of ions. The fourth and most widely accepted mechanism is dissociative recombination. The last four reactions in this mechanism,

$$H_3O^+ + e^- \rightarrow H_2O + H,$$

$$C_3H_3^+ + e^- \rightarrow \text{products},$$

$$CH_3^+ + e^- \rightarrow CH_2 + H,$$

and

$$C_2H_3O^+ + e^- \rightarrow M + H.$$

are dissociative recombination reactions. They provide the path for four of the five ions considered in the ionic mechanism. The reverse of the chemiionization reactions is the dissociative recombination path for the fifth ion, CHO^+.

Reaction rate coefficients have been measured for only a limited number of ion-molecule reactions [45]. These coefficients are estimated from the average dipole orientation (ADO) theory [46, 47, 48] for reactions in which experimental data does not exist. The ADO theory predicts a temperature dependent rate coefficient which is correlated to the parametric rate expression

$$k = AT^{-n}. \tag{3.1}$$

The values of n range from 0.006 to 0.09.

No negative ions are included in the model since it has been observed that approximately 99% of the negative ions present are free electrons [9].

3.3 Calculation of the Reverse Reaction Rates

The reverse reaction rates are calculated using the chemical equilibrium coefficient, K_{eq}, defined by

$$K_{eq} = \frac{k_f}{k_r} = e^{-\frac{\Delta G}{RT}} \tag{3.2}$$

where

$$\Delta G = \left[\sum_{i=1}^{P} G_i\right]_{products} - \left[\sum_{i=1}^{R} G_i\right]_{reactants}. \tag{3.3}$$

The thermochemical data needed for calculating the properties of neutral species are taken from the JANAF tables [49]. Estimated values for the heat of formation for the ions are listed in Table 3.2.

Ideally, the expression for the reaction rates would take the form of the modified Arrhenius equation,

$$k = AT^B e^{-\frac{E_a}{RT}}. \tag{3.4}$$

Table 3.2: Heats of formation for each ion in kcal/mole

Species	ΔH_f°	Reference
H_3O^+	139.0	[49]
CH_3^+	256.0	[50]
CHO^+	199.1	[49]
$C_3H_3^+$	255.0	[32]
$C_2H_3O^+$	151.0	[51]

This gives the rates of reaction as a function of temperature. The coefficients A, B, and E_a are unknowns. For a specified range of temperatures, ΔG is tabulated. The reverse reaction rate is then calculated using this value at each temperature. A least square analysis is then used to compute the coefficients A, B, and E_a of the modified Arrhenius equation (Eqn. (3.4)).

4. THEORY

4.1 Governing Equations

The flame simulated in this work is a one-dimensional laminar premixed flame. A flat flame burner is usually used to simulate this type of flame in the laboratory. A drawing of a typical flat flame burner is in Figure 4.1. The fuel and oxidant flow uniformly from the burner in the vertical direction. The flame is stabilized above the burner and below the positive electrode. The symmetry of the flame allows for a one-dimensional analysis to be used in this research.

The equations describing a one-dimensional laminar premixed flame in the presence of an electric field include the mass and species conservation equations, and Poisson's equation to describe the electric field intensity.

Mass conservation:

$$\frac{\partial \rho}{\partial t} + \frac{\partial (\rho u)}{\partial x} = 0 \tag{4.1}$$

Species conservation:

$$\rho \frac{\partial Y_i}{\partial t} + \rho u \frac{\partial Y_i}{\partial x} = -\frac{1}{A} \frac{\partial (A J_i)}{\partial x} + \omega_i \tag{4.2}$$

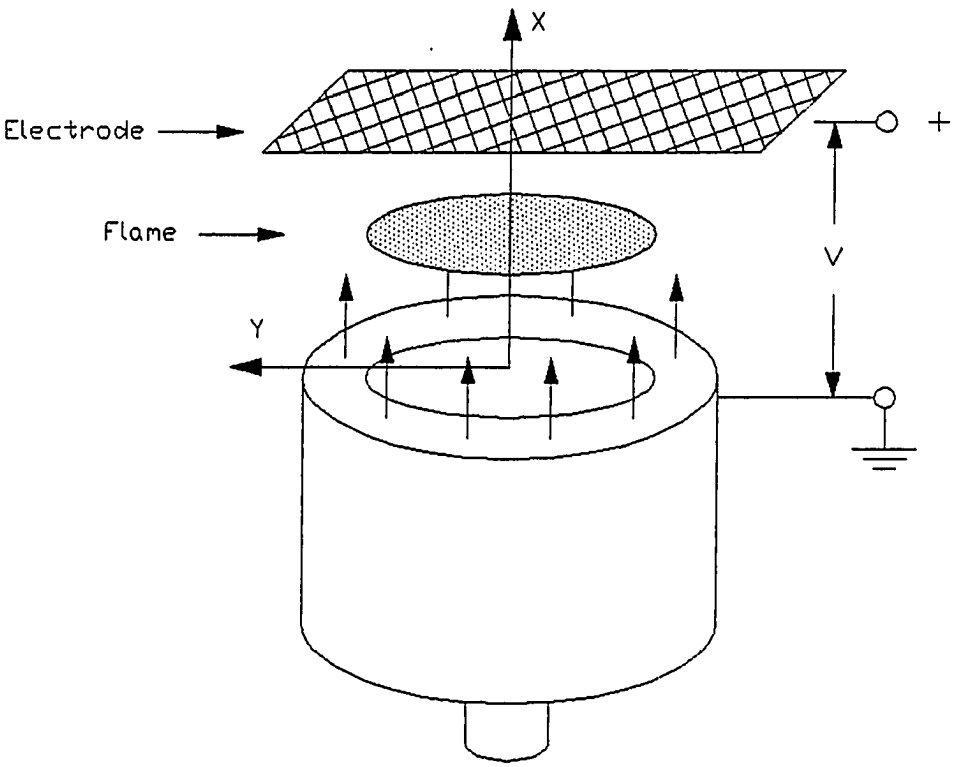

Figure 4.1: Diagram of a typical flat flame burner

Poisson's Equation:

$$\frac{d^2V}{dx^2} = -\frac{1}{\epsilon_o}(n_+ - n_-)e \tag{4.3}$$

where V is the voltage, ϵ_o is the permissivity constant, e is the electron charge, and n_+ and n_- are positive and negative ion concentrations, respectively. The unsteady terms in the conservation equations are retained as a computational device only. This allows for a steady state solution to be reached by stepping through time until the time derivatives equal zero. This approach to solving the conservation equations was proposed by Spalding and Stephenson [52].

The pressure throughout the flame is assumed to be nearly constant. Because of the zero pressure drop, the momentum equation does not need to be solved. Since experimental temperature profiles are used, it is not necessary to solve the energy equation.

The forces imparted on a neutral gas by an ion is a result of the charge carrier moving down a potential gradient. This causes the ion to increase in energy. Since its own kinetic energy cannot increase (due to a constant mobility) it must be dissipated to the neutral gas. This force per unit volume, F, is described by

$$F = Ee(n_+ - n_-). \tag{4.4}$$

Substituting the expression for current flux

$$j = Een_{\pm}\mu_{\pm} \tag{4.5}$$

into Equation (4.4) gives an expression for the force per unit volume in terms of mobility and current:

$$F = j\left(\frac{1}{\mu_+} - \frac{1}{\mu_-}\right). \tag{4.6}$$

Multiplying Equation (4.6) by the distance from the flame to an electrode will give an expression for the pressure drop across the flame:

$$\Delta p = jx\left(\frac{1}{\mu_+} - \frac{1}{\mu_-}\right). \tag{4.7}$$

Lawton and Weinberg [36] predict the maximum ΔP, from Equation (4.7), to be on the order of 0.0004 atmosphere. The resulting force is small in magnitude compared to the terms in the energy and species conservation equations. This is the basis for neglecting ionic wind effects in the flame.

The mass flux, J_i, is obtained from the summation of the Stefan-Maxwell equations for normal and thermal diffusion [53]:

$$J_i = \frac{c^2}{\rho} M_i \sum_{\substack{j=1 \\ j\neq 1}}^{nspc} M_i D_{i,j} \frac{\partial X_i}{\partial x} - D_{i,T} \frac{\partial \ln T}{\partial x}. \tag{4.8}$$

Blanc's law allows a simplified approach to be used for the calculation of J_i [53]:

$$J_i = -\rho D_{i,m} \frac{\partial Y_i}{\partial x} - D_{i,T} \frac{\partial \ln T}{\partial x} \tag{4.9}$$

where

$$D_{i,m} = \frac{1 - Y_i}{\sum_{\substack{j=1 \\ j\neq i}}^{nspc} \frac{X_i}{D_{i,j}}} \tag{4.10}$$

and

$$D_{i,T} = k_{i,m} \rho Y_i \frac{1 - Y_i}{\left(X_i \sum_{\substack{j=1 \\ j\neq i}}^{nspc} \frac{X_j}{D_{ij}}\right)}. \tag{4.11}$$

Warnatz [53] has shown the simplified approach for calculating mass and thermal diffusion is accurate to within a few percent of the exact solution of the Stefan-Maxwell equations. In this study, thermal diffusion is calculated only for H and H_2 because these are the smallest molecules and have the largest thermal diffusion rates.

To account for the mobility in an external electric field, an additional term must be added to the mass flux for the ionic mechanism.

$$J_i' = -D_{i,m}\rho\frac{\partial Y_i}{\partial x} - D_{i,T}\frac{\partial \ln T}{\partial x} + \mu_{i,m}\rho Y_i E. \tag{4.12}$$

The mobility, μ, can be related to diffusion by the Einstein relationship [54]:

$$\frac{D_{i,j}}{\mu_{i,j}} = \frac{kT}{e} = T \times 8.617 \times 10^{-5}. \tag{4.13}$$

Little experimental data are available on the diffusion of ions. Because of this, it is assumed that the diffusivity of ions is equal to that of the corresponding neutral species. From these assumed ion diffusion coefficients, the mixture mobility, $\mu_{i,m}$, can be determined [54]:

$$\mu_{i,m} = \left(\sum_{\substack{j=1 \\ j\neq i}}^{nspc} \frac{X_i}{\mu_{i,j}} \right)^{-1} \quad cm^{-1}V^{-1}s^{-1}. \tag{4.14}$$

The mobility of ions in nitrogen at 1000 K is approximated by [54]

$$\mu_e \approx \frac{2.0 \times 10^{22}}{n} \quad cm^{-1}V^{-1}s^{-1} \tag{4.15}$$

where n is the electron density. The diffusion coefficient for electrons can then be determined by rearranging the Einstein relationship.

$$D_e = 8.93 \times 10^3 \quad \frac{cm^2}{s}. \tag{4.16}$$

The diffusivity is assumed to scale with temperature to the $\frac{3}{2}$ power [36]. This (Eqn.(4.16)) leads to an expression for electron diffusion as a function of temperature:

$$D_e = 0.2824 \times T^{\frac{3}{2}} \quad \frac{cm^2}{s}. \tag{4.17}$$

In the absence of more complete data, this relationship is used to estimate electron diffusion in this work.

In general, the diffusion coefficients for positive and negative ions are different. An extreme disparity in diffusion rates occurs when the negative charge is carried by free electrons because diffusivity increases with decreasing mass. The resulting charge separation is opposed by a self-induced electric field that increases as the charge separation becomes larger. Eventually the faster charges are so retarded by the electric field that both the positive ions and electrons diffuse at the same rate in a process known as ambipolar diffusion [36].

In past research, the ambipolar diffusion coefficient was found by expression:

$$D_a = \frac{D_+\mu_- + D_-\mu_+}{\mu_+ + \mu_-} \tag{4.18}$$

This research introduces a alternative method for calculating the mobility and hence the ambipolar diffusion coefficient. Poisson's equation (Eqn. 4.3) is solved to give the electric field distribution throughout the flame. This is a function of the net charge density within the flame. The mobility for the positive ions can be calculated from Equation (4.14) which is a function of ion density. Accordingly, the effects of charge separation are accounted for explicitly rather than by use of ambipolar diffusion coefficients.

To simplify the conservation equations by eliminating the convection terms and automatically satisfying continuity, a coordinate transformation [12] is made using

$$\frac{\partial \psi}{\partial x} = \rho \quad and \quad \frac{\partial \psi}{\partial t} = -\rho u. \tag{4.19}$$

The general form of the resulting equation for the neutral species mechanism is

$$\rho \frac{\partial \varphi}{\partial t} = \rho \frac{\partial}{\partial \psi}(\rho \Gamma \frac{\partial \varphi}{\partial \psi}) + G \tag{4.20}$$

where the expressions corresponding to Γ and G are in Table 4.1 [12]. The transformed equation for the ionic species mechanism is

$$\rho\frac{\partial\varphi}{\partial t} = \rho\frac{\partial}{\partial\psi}\left(\rho\Gamma\frac{\partial\varphi}{\partial\psi}\right) + \rho\frac{\partial}{\partial\psi}(\rho\Gamma') + G \tag{4.21}$$

where the expressions corresponding to Γ, Γ', and G are also in Table 4.1. The appropriate boundary conditions are

$$\varphi = \varphi_0 \quad at \quad \psi = 0 \tag{4.22}$$

and

$$\frac{\partial\varphi}{\partial\psi} = constant \quad at \quad \psi = \infty. \tag{4.23}$$

The variable φ is a generic term for the mass fraction Y_i and ψ is the transformed spatial variable.

Table 4.1: Values of Γ, Γ' and G for the species consveration equations

Equation	Γ	Γ'	G
Neutral model	$D_{i,m}\rho$	—	ω_i
Ionic model	$D_{i,m}\rho$	$-\mu_{i,m}\rho Y_i E$	ω_i

Solving Equations (4.20) and (4.21) using the above boundary conditions gives the solution in the ψ coordinate system. A simple transformation back to the x coordinate system is obtained by a rearrangement of Equation (4.19),

$$x = \int_{\psi=0}^{\psi} \frac{d\psi}{\rho}. \tag{4.24}$$

4.2 Computation Method

4.2.1 Solution process

Solving Equations (4.20) and (4.21) numerically is difficult because of stiffness introduced by the chemical generation term G. This is due to the fact that G may vary by orders of magnitude in the problem domain. This problem can be circumvented by using a split operator technique [11, 55, 56] that will divide Equation (4.20) into two equations and Equation (4.21) into three equations. The first part consists of the equation

$$\rho\frac{\partial\varphi}{\partial t} = G \tag{4.25}$$

and

$$\rho\frac{\partial\varphi}{\partial t} = \rho\frac{\partial}{\partial\psi}\left(\rho\Gamma\frac{\partial\varphi}{\partial\psi}\right) \tag{4.26}$$

for both models. The third equation, which is exclusively for the ionic model, includes ion mobility:

$$\rho\frac{\partial\varphi}{\partial t} = \rho\frac{\partial}{\partial\psi}(\rho\Gamma') \tag{4.27}$$

Equations (4.25) and (4.26) represent the time rate of change of φ due to transport and chemical generation. These equations are the same for both the neutral and ionic mechanisms. The time rate of change of φ due to ion mobility is described by Equation (4.27) and is only solved when φ is the mass concentration of an ionic species.

Equations (4.25)–(4.27) are PDEs in time and space. Partial differential equations are more difficult to solve than ODEs. Therefore, a special algorithm called TRANSEQI [12] is modified to make the equations more tractable.

The iterative technique introduced in TRANSEQI is used as the basis for the development of the computer code for this research. TRANSEQI uses the method of lines [12] to convert the PDEs into ODEs. The ODEs are then solved using a commercial integrator. The approach used in this work utilizes common finite difference techniques as well as integration software packages. The generation equation (Eqn. (4.25)) is solved using LSODE [55]. The boundary condition at ψ=0 is described by

$$\frac{\partial \varphi}{\partial t} = 0 \tag{4.28}$$

and

$$\frac{\partial \varphi}{\partial t} = \left(\frac{G}{\rho}\right) \tag{4.29}$$

at ψ=∞.

To ensure stability, a simple implicit method is used to solve the diffusion equation (Eqn. (4.26)) which takes the form of

$$\varphi_i^{n+1} = \frac{\Delta t}{\Delta \psi^2}[\rho^n_{\frac{i+1}{2}} \Gamma^n_{\frac{i+1}{2}} (\varphi_{i+1}^{n+1} - \varphi_i^{n+1}) - \rho^n_{\frac{i-1}{2}} \Gamma^n_{\frac{i-1}{2}} (\varphi_i^{n+1} - \varphi_{i-1}^{n+1})] + \varphi_i^n. \tag{4.30}$$

The notations $\rho_{\frac{i+1}{2}}$, $\rho_{\frac{i-1}{2}}$, $\Gamma_{\frac{i+1}{2}}$ and $\Gamma_{\frac{i-1}{2}}$ are computed using

$$\rho_{\frac{i\pm1}{2}} = \frac{\rho_i + \rho_{i\pm1}}{2} \tag{4.31}$$

and

$$\Gamma_{\frac{i\pm1}{2}} = \frac{\Gamma_i + \Gamma_{i\pm1}}{2}. \tag{4.32}$$

The boundary condition at ψ=0 is

$$\varphi_1^{n+1} = \varphi_1^n \tag{4.33}$$

and

$$\varphi_N^{n+1} = \frac{2\Delta t}{\Delta\psi^2}[\rho^n_{\frac{N-1}{2}}\Gamma^n_{\frac{N-1}{2}}(\varphi_N^{n+1} - \varphi_{N-1}^{n+1})] + \varphi_N^n \tag{4.34}$$

at $\psi=\infty$. The Thomas algorithm is used to solve the resulting tridiagonal set of equations. The matrices solved have dimensions of NxN where N is the number of nodes.

Equation (4.30) is valid for uniformly spaced grids. Throughout this research, the ratio of any two consecutive grid lengths does not vary significantly from unity. Therefore, the error introduced in using this simple implicit method for a nonuniform mesh is negligible.

A simple explicit scheme is utilized in the solution of the ion mobility equation (Eqn. (4.27)). Stability is not an issue since the time increment used for the generation equation is too small to induce instabilities. Discretizing Equation (4.27) results in

$$\varphi_i^{n+1} = \Delta t\left[\frac{\rho^n_{i+1}\Gamma'^n_{i+1} - \rho^n_i\Gamma'^n_i}{\Delta\psi}\right] + \varphi_i^n \tag{4.35}$$

with

$$\varphi_1^{n+1} = \varphi_1^n \tag{4.36}$$

and

$$\varphi_N^{n+1} = \Delta t\left[\frac{\rho^n_N\Gamma'^n_N - \rho^n_{N-1}\Gamma'^n_{N-1}}{\Delta\psi}\right] + \varphi_N^n \tag{4.37}$$

at the $\psi=0$ and $\psi=\infty$ boundaries respectively. This results in the simultaneous solution of N equations.

Estimated species profiles are used as initial conditions in the algorithm. The transport coefficients and molar production rates are calculated for each species at each nodal point based on these initial conditions. The transport equation for the first species is solved holding all species concentrations constant for one time increment. If

the current species is an ionic species, the ion mobility equation is solved holding all other species concentrations constant for one increment in the time step. At the next time step, the generation equation for the same species is solved. All other species concentrations are again held constant throughout the integration. The resulting $\Delta\varphi$ from the transport, ion mobility, and chemical generation equations are added to the input φ. This gives the new φ value that is used in subsequent integrations. The transport, ion mobility, and generation equations are then solved in the same manner for each of the remaining species. Property and mixture coefficients are then calculated using the new values of temperature and species concentrations. The evaluation of property and mixture coefficients can be updated periodically rather than at the end of each time step, which helps reduce the number of computations executed in the program. This methodology is repeated until all time derivatives approach zero. Stiffness is virtually eliminated since only one species is treated at any one time by the integrator.

Poisson's equation (Eqn. (4.3)) must also be solved since ionic species are included in the mechanism. This allows for the evaluation of the electric field distribution. After one complete iteration of all of the species, Poisson's equation (Eqn. (4.3)) is solved. Like the transport coefficients, Poisson's equation can be solved periodically to help reduce computer time. To transform Poisson's equation (Eqn. (4.3)) into a first order ODE, it is rewritten in state variable form by defining the electric field intensity $E = -\frac{dV}{dx}$ and substituting into Equation (4.3):

$$\frac{dE}{dx} = \frac{1}{\epsilon_0}(n_+ - n_-)e \tag{4.38}$$

and

$$\frac{dV}{dx} = -E \tag{4.39}$$

with V(x=0) and V(x=L) as prescribed boundary conditions. The resulting boundary value problem is solved using a shooting method described in Appendix A. This iteration technique is depicted by the flow chart in Figure 4.2.

Flow simulations are performed on a HDS AS/9160. The number of grid points used for the simulations range from 50 to 70. The average CPU time required to reach steady state using the modified TRANSEQI iteration technique is 20 minutes. The CPU times reported in this work are, on average, a factor of 10 faster than the CPU times reported by Pedersen [57] for similar methane flame simulations. In his work, Pedersen [57] used the original form of TRANSEQI introduced by Eraslan and Brown [12].

4.2.2 Adaptive grid algorithm

Smooke *et al.* [58] have shown that by concentrating the grid points in areas of steep temperature gradients, computer time and accuracy can be improved for flame calculations. Therefore, an adaptive grid generator is used to produce a larger concentration of nodes in areas of large temperature gradients. A variation in the method proposed by Dwyer and Sanders [59] is used throughout this work. By letting the grid interval Δx_i, be defined as [58]

$$\Delta x_i = \frac{L \sum_{n=1}^{i} \left[1 + \frac{B}{1 + \left| \frac{\partial \varphi}{\partial x} \right|_n} \right]}{\sum_{n=1}^{N} \left[1 + \frac{B}{1 + \left| \frac{\partial \varphi}{\partial x} \right|_n} \right]}, \tag{4.40}$$

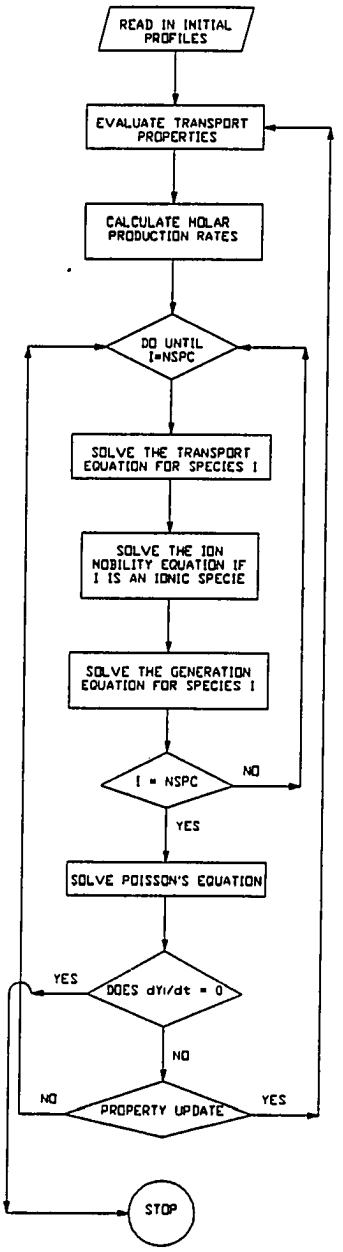

Figure 4.2: Flow chart of the iteration technique used in this research

where L is the domain length and B is the stretching parameter. The stretching parameter must be greater than zero for nonuniform grid spacing and equal to zero for equi-spacing. An increase in B results in an increase in the ratio of Δx_{max} to Δx_{min}.

4.2.3 Estimation of initial conditions

Good initial estimates of concentration and temperature profiles can result in substantial decreases in computation time. These initial profiles can be generated via a simple procedure developed by Goyal *et al.* [56]. It is based on conservation of atomic elements and the assumption that enthalpy is constant throughout the flame region.

Initially a temperature profile is needed. Experimental profiles were used in this study. The use of experimental temperature profiles allows the model to correctly account for heat losses. These losses can be attributed to radiative, convection, and conduction heat transfer. The radical species profiles are then determined using

$$Y_i = Y_i^c + (Y_i^h - Y_i^c)\tau \tag{4.41}$$

where

$$\tau = \frac{T - T^c}{T^h - T^c}. \tag{4.42}$$

Superscripts c and h refer to the cold and hot regions of the flame.

Mass fraction profiles for major species are then calculated based on atomic element conservation and constant enthalpy. The result is a set of linear equations described by

$$H^c = \sum_{i=1}^{nspc} h_i Y_i \tag{4.43}$$

$$Y_{ei}^{c} = \sum_{j=1}^{nspc} Y_j a_{i,j} \tag{4.44}$$

where Y_{ei} is the mass fraction of element i in the mixture and $a_{i,j}$ is the mass fraction of element i in species j. When Equations (4.41),(4.43), and (4.44) are combined they form a set of simultaneous linear algebraic equations. A simple computer code is used to generate these profiles.

The lack of ionic species and minor neutral species data prevent the estimation of some concentration profiles. In these cases, the initial concentration profiles for the species are set to zero.

4.2.4 Transport and mixture coefficients

All transport and mixture coefficients are calculated via PROP, which is a collection of FORTRAN subroutines for calculating gas mixture properties [60]. The relationships describing thermal conductivity, mixture diffusivity, thermal diffusivity, mixture densities, and mixture specific heats are:

$$\lambda = \frac{1}{2}\left[\sum_{i=1}^{nspc} X_i\lambda_i + \left(\sum_{i=1}^{nspc} \frac{X_i}{\lambda_i}\right)^{-1}\right], \tag{4.45}$$

$$D_{i,m} = \frac{1 - Y_i}{\left(\sum_{\substack{i=1 \\ i\neq j}}^{nspc} \frac{X_j}{D_{ij}}\right)}, \tag{4.46}$$

$$D_{i,T} = k_{i,m}\rho Y_i \frac{1 - Y_i}{\left(X_i \sum_{\substack{j=1 \\ j\neq i}}^{nspc} \frac{X_j}{D_{ij}}\right)}, \tag{4.47}$$

$$\rho = \frac{P}{RT}\left(\sum_{i=1}^{nspc} \frac{Y_i}{M_i}\right)^{-1}, \tag{4.48}$$

and

$$C_p = \sum_{i=1}^{nspc} C_{p_i} \left(\frac{Y_i}{M_i} \right). \tag{4.49}$$

The estimation of the individual species thermal conductivity, λ_i, and binary diffusion coefficients are shown in detail in Appendix B. The mixture and transport coefficients are calculated at each grid point and updated periodically throughout the integration.

5. RESULTS AND DISCUSSIONS

5.1 Lean Methane Flame Simulations

5.1.1 Neutral species

The lean flame case study used to validate the methane mechanism in this research is for an equivalence ratio of 0.2. A pressure of 40 torr is used for the simulation. The simulation results are shown in Figures 5.1–5.5. The experimental data shown in the figures are from Peeters and Mahnen [61]. The CH_4, O_2, H_2O, CO, and CO_2 profiles in Figures 5.1 and 5.2 show excellent agreement with the experimental data. The simulation and experimental results for CH_3, H, H_2, O, HO_2, and CH_2O differ from each other by up to 45% which is within the uncertainty of the experimental results. The model overpredicts the experimental data in the post flame region.

Olsson and Andersson [62] performed a sensitivity study on a lean (Φ=0.2), low pressure (40 torr) methane/oxygen flame. Their study indicated that small perturbations in the reaction rates for reactions that produce CO from CHO could result in variations of up to 50% in the some species concentrations. The concentration profiles for CH_3, H, H_2, O, HO_2, and CH_2O were found to be sensitive to changes in the reaction rates for

$$CHO + M' \rightarrow H + CO + M'.$$

The reaction rate for this particular reaction has a high degree of uncertainty associated with it [63]. Olsson and Andersson [62] showed that by increasing the reaction rate by a factor of five, well within its range of uncertainty, would produce changes in the concentrations of the aforementioned species in an excess of up to 50%.

Considering the sensitivity of the species profiles to the rate of this reaction, it can be concluded that the predicted concentration profiles are in good agreement with the experimental data.

5.1.2 Ionic species

Goodings *et al.* [35] used a mass spectrometer to determine the total ion current for a methane/oxygen flame at 760 torr and an equivalence ratio of 0.2. The experimental profiles are shown in Figure 5.6. The ion concentration profiles predicted by the model, shown in Figure 5.7, are for a lean flame (Φ=0.2) at a pressure of 40 torr. This will allow for a qualitative comparison to be made between the experimental and predicted profiles.

The model predicted H_3O^+ to be the dominant ion with an ion density of $5x10^{10}/cm^3$. The peak value of this ion occurs slightly downstream of the peak concentrations of the other ions. The slower decay of this ion is attributed to the reaction

$$CHO^+ + H_2O \rightarrow H_3O^+ + CO,$$

which produces the majority of the H_3O^+ ions in a region where there is a rapid increase in the production of H_2O. The other major ions have associated with them a more rapid decay. This is due to the fact that these ions are formed by reaction intermediates that decrease rapidly in concentration through the flame. These general

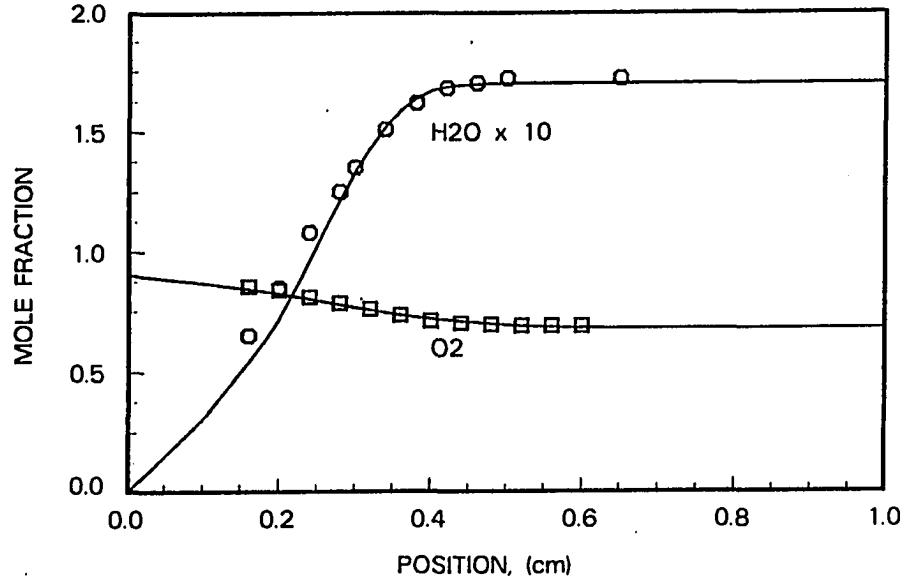

Figure 5.1: Predicted and experimental profiles for H_2O and O_2 for a CH_4/O_2 flame (Φ=0.2). The experimental data are denoted by symbols [61]

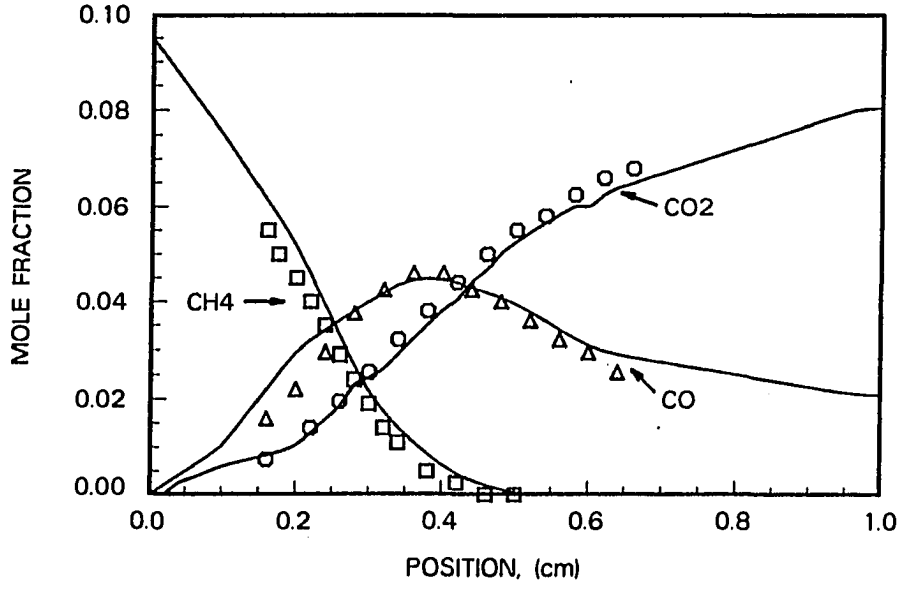

Figure 5.2: Predicted and experimental profiles for CH_4, CO, and CO_2 for a CH_4/O_2 flame (Φ=0.2). The experimental data are denoted by symbols [61]

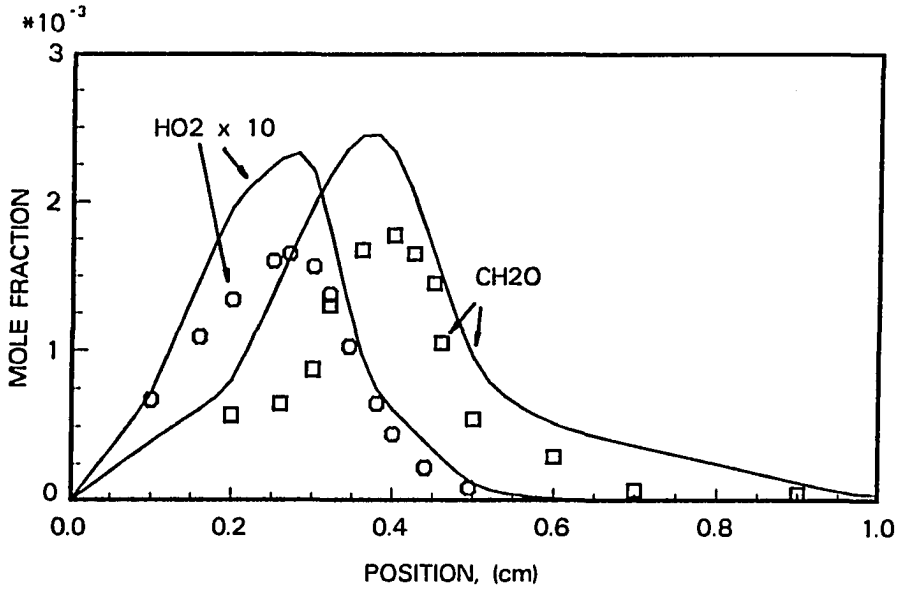

Figure 5.3: Predicted and experimental profiles for HO_2 and CH_2O for a CH_4/O_2 flame (Φ=0.2). The experimental data are denoted by symbols [61]

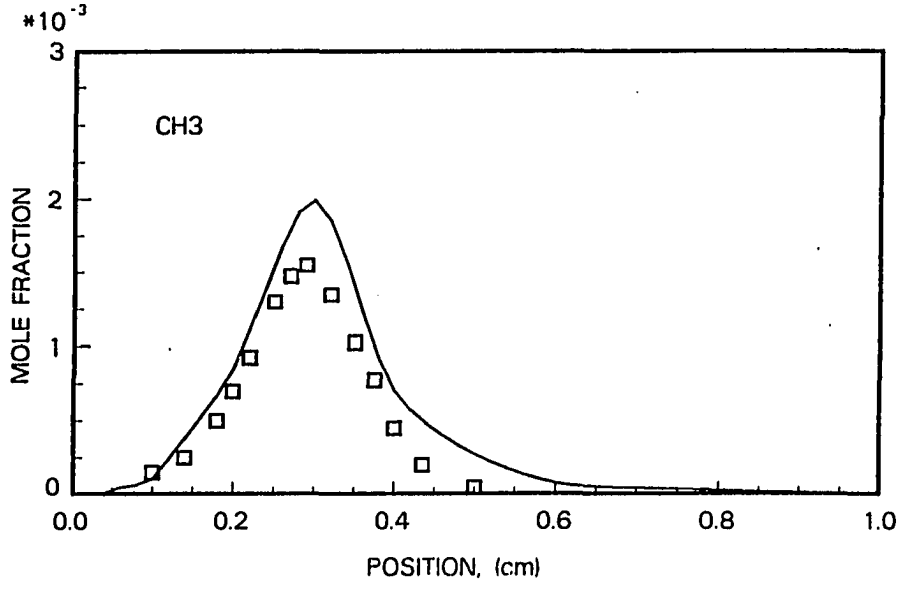

Figure 5.4: Predicted and experimental profiles for CH_3 for a CH_4/O_2 flame (Φ=0.2). The experimental data are denoted by symbols [61]

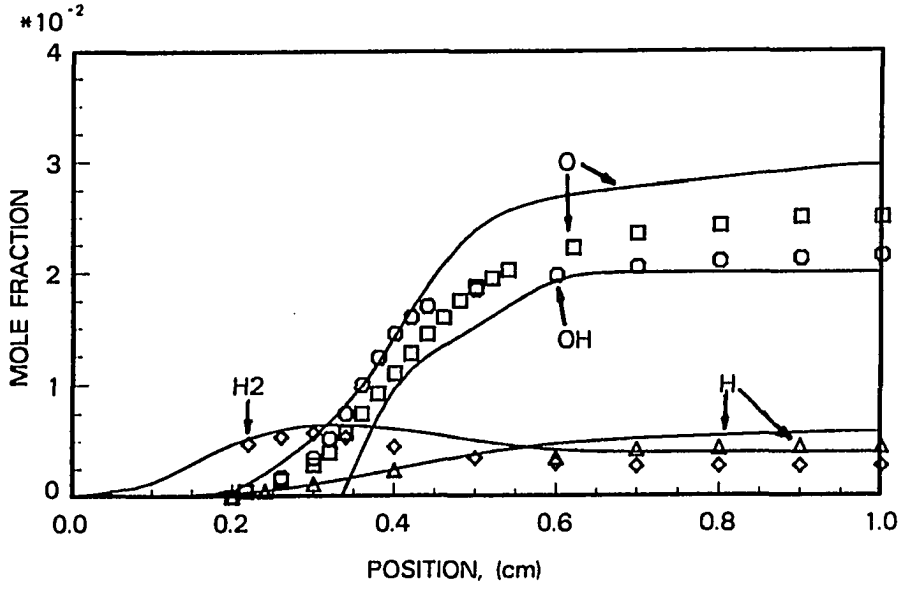

Figure 5.5: Predicted and experimental profiles for H, H_2, O, and OH for a CH_4/O_2 flame (Φ=0.2). The experimental data are denoted by symbols [61]

features of the ion profiles agree with experimental data obtained from Goodings *et al.* [35]. Calcote [64] found this slow decay of H_3O^+ ions and rapid decay of the other major ions to be true for hydrocarbon flames in general.

The predicted ratio of the peak ion concentrations to the total ion concentration for the major ions are shown in Table 5.1. The experimental ratio of the peak ion signal to the total ion signal are also shown in the same table. This will allow for a qualitative comparison to be made between the peak experimental and predicted ion values.

The ratio of the maximum value of H_3O^+ and $C_2H_3O^+$ to the total ion concentration predicted by the model compare well with the experimental values. However, the predicted concentration of CH_3^+ underpredicts the experimental value by factor

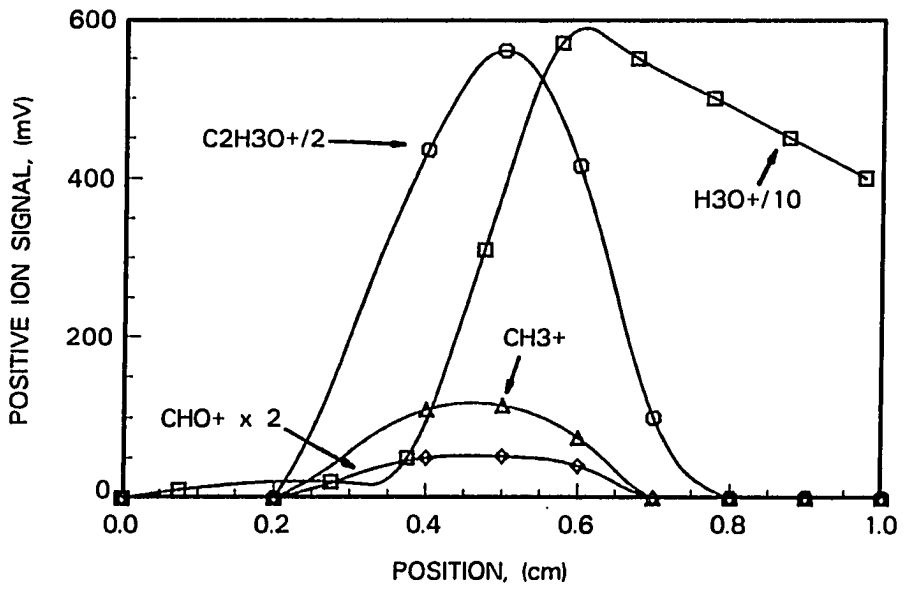

Figure 5.6: Experimental ion profiles for for a lean CH_4/O_2 flame (Φ=0.2) [35]

of two. The underprediction of CH_3^+ is thought to be related to the overprediction of $C_3H_3^+$ by the reaction

$$CH_3^+ + C_2H_2 \rightarrow C_3H_3^+ + H_2.$$

The abundance of C_2H_2 produces an excess of $C_3H_3^+$ at the expense of CH_3^+. The overprediction of CH_3 indirectly caused by the reaction

$$CHO + M' \rightarrow H + CO + M'$$

is responsible for this abundance of C_2H_2. This reaction is also responsible for a large concentration of CH which causes an overprediction of the CHO^+ ion.

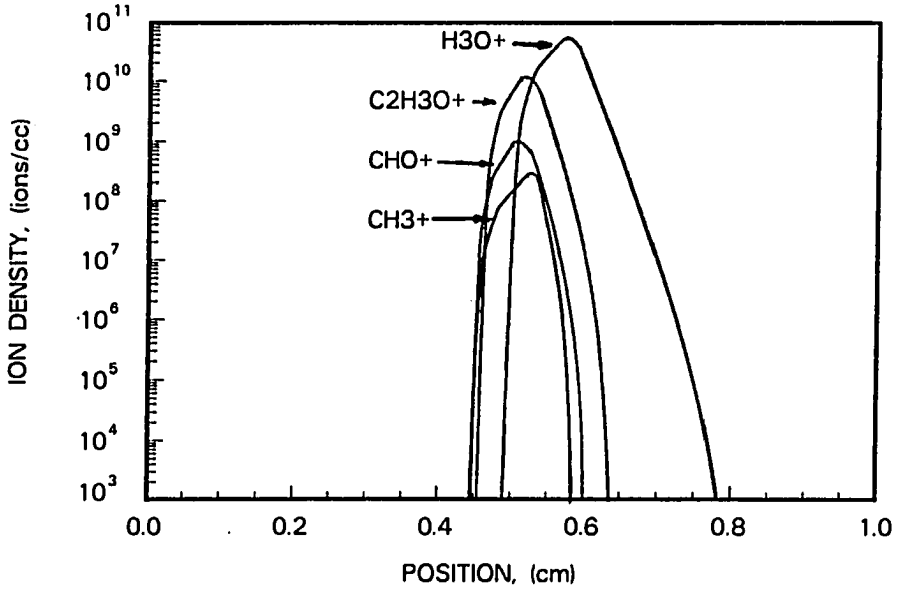

Figure 5.7: Predicted ion profiles for for a lean CH_4/O_2 flame (Φ=0.2)

5.2 Stoichiometric Methane Flame Simulations

5.2.1 Neutral species

Species concentrations predicted by the methane mechanism for a stoichiometric flame (Φ=1.0) are compared to experimental results. The experimental data are taken from Bechtel *et al.* [1] for a flame at atmospheric pressure and an unburnt gas temperature of 298 K. The O_2, H_2O, and temperature profiles are in Figure 5.8. The model accurately predicts the measured O_2 and H_2O profiles. Figure 5.9 shows the H_2 and CO profiles to have peak concentrations in the flame front with lower concentrations in the burnt gas region. The general trend of the predicted profiles agree with the experimental data. However, the peak concentration of the predicted CO profile falls short of the measured value. Bechtel *et al.* [1] indicate the error

Table 5.1: Experimental [35] and predicted ratios of the peak ion concentration to total ion concentration for a lean CH_4/O_2 flame

	$\frac{\text{peak ion signal}}{\text{peak total ion signal}}$	$\frac{\text{peak ion concentration}}{\text{peak total ion concentration}}$
Species	experimental	predicted
H_3O^+	0.804	0.770
$C_2H_3O^+$	0.158	0.182
CH_3^+	0.023	0.011
CHO^+	0.004	0.036
$C_3H_3^+$	—	0.0001

associated with the peak value of CO is ±10%. Therefore this difference can be attributed to experimental scatter. The predicted and measured concentrations of CH_4 and H_2O in Figure 5.10 show good agreement between each other.

5.2.2 Ionic species

Peeters *et al.* [65] have investigated ion concentrations for stoichiometric CH_4/O_2 flames at atmospheric pressure. Figure 5.11 contains the ion concentration profiles obtained from the computer model and Figure 5.12 contains the experimental ion concentration profiles. The major ion, H_3O^+, shows a delayed peak in concentration compared to the CHO^+, $C_3H_3^+$, and $C_2H_3O^+$ profiles. The H_3O^+ profile generally exhibits this type of behavior in hydrocarbon flames. The remaining ions peak in the flame front and then rapidly disappear. Again, this is due to the rapid production and then consumption of reaction intermediates in the flame region. It is these reaction intermediates that create CHO^+, $C_3H_3^+$, and $C_2H_3O^+$. The general trends agree with

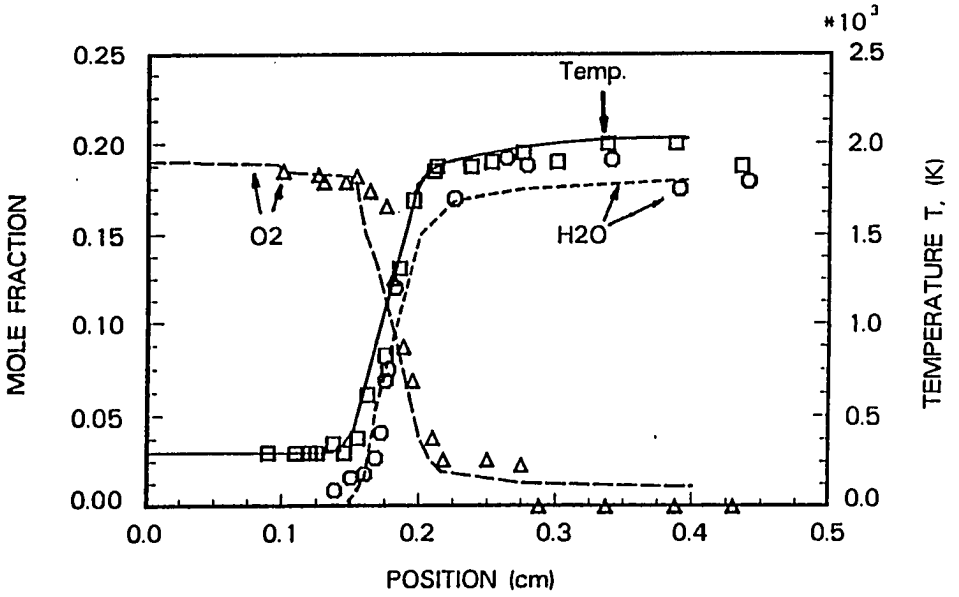

Figure 5.8: Predicted and experimental profiles for O_2, H_2O, and temperature for a CH_4/air flame (Φ=1.00). The experimental data are denoted by symbols [1]

experimental results obtained by Peeters *et al.* [65].

Table 5.2 lists the peak ion density values for H_3O^+, CHO^+, $C_3H_3^+$, and $C_2H_3O^+$. The predicted peak concentrations for these four ions are within a factor of four of their experimental counterparts. The final flame temperature used in the simulations is 2240 K. Peeters *et al.* [65] document a range of final flame temperatures varying from 1830 to 2084 K. In the same paper, Peeters *et al.* [65] show the ion yield to increase approximately 20% per 75 K increase in temperature. Therefore, the difference in flame temperature can be held responsible for the discrepancies in the ion concentrations.

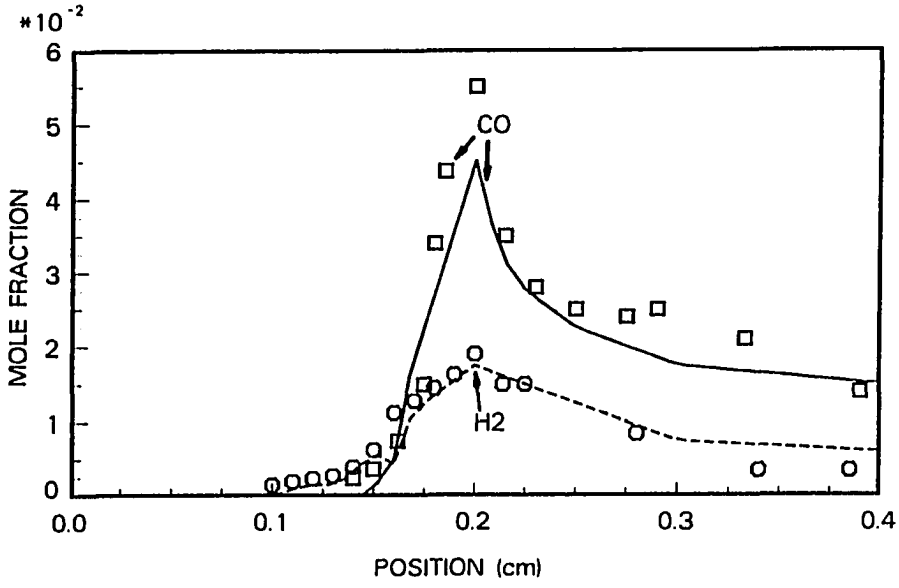

Figure 5.9: Predicted and experimental profiles for H_2 and CO for a CH_4/air flame (Φ=1.00). The experimental data are denoted by symbols [1]

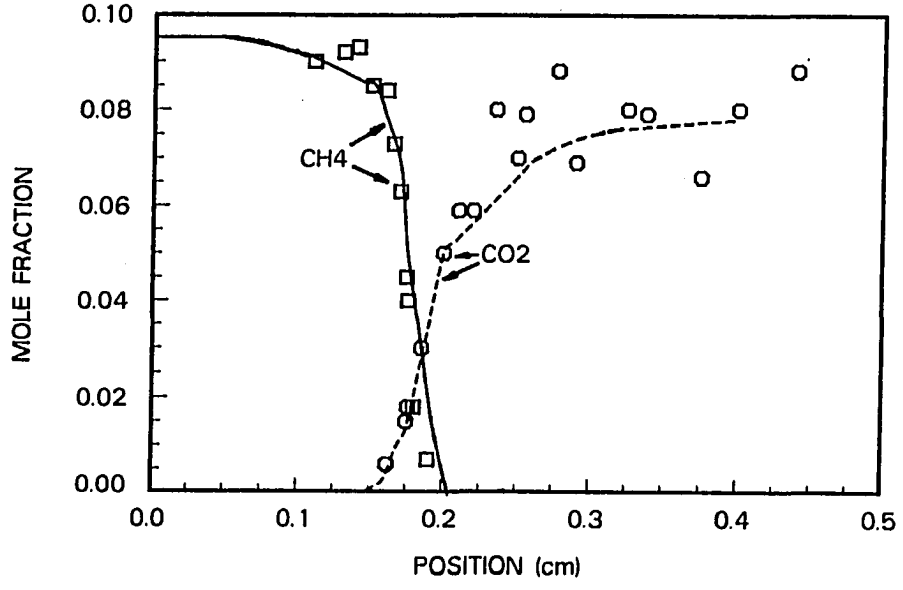

Figure 5.10: Predicted and experimental profiles for CH_4 and CO_2 for a CH_4/air flame (Φ=1.00). The experimental data are denoted by symbols [1]

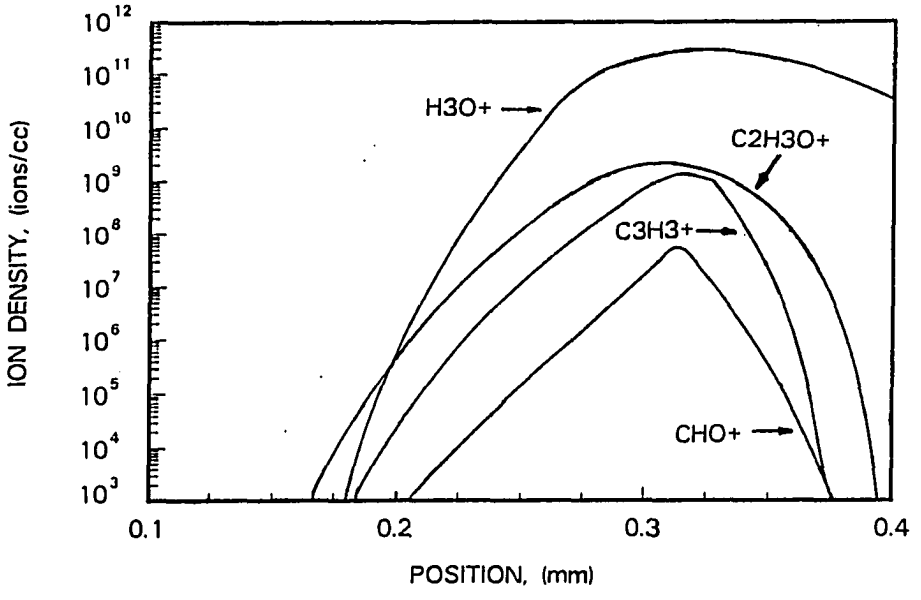

Figure 5.11: Predicted ion profiles for a CH_4/O_2 flame (Φ=1.00)

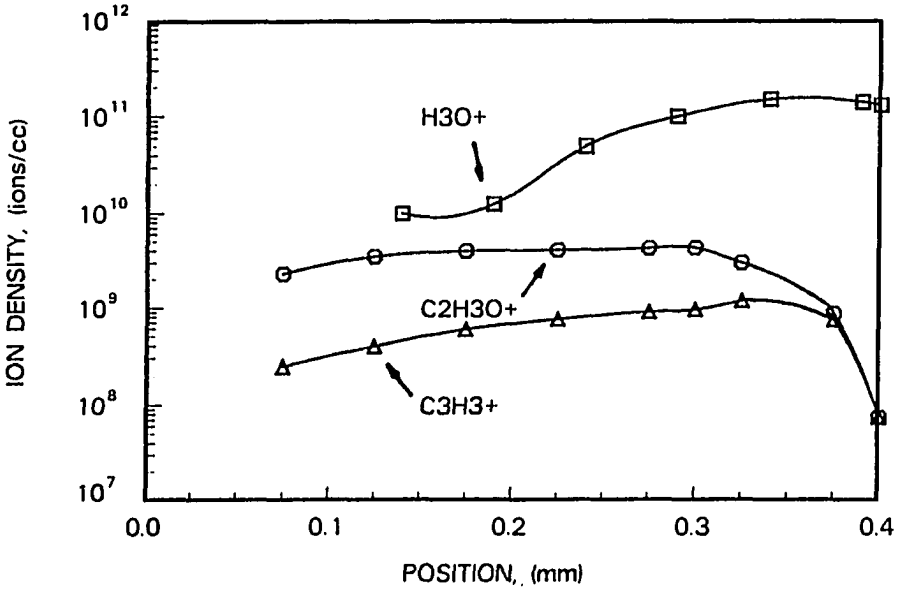

Figure 5.12: Experimental ion profiles for a CH_4/O_2 flame (Φ=1.00) [65]

Table 5.2: Experimental [65] and predicted peak ion densities (ions/cm^3) for a stoichiometric CH_4/O_2 flame

Species	Peak ion density$_{exp}$	Peak ion density$_{pred}$
H_3O^+	1.5×10^{11}	3.1×10^{11}
$C_2H_3O^+$	4.3×10^{9}	2.0×10^{9}
$C_3H_3^+$	1.2×10^{9}	1.5×10^{9}
CHO^+	1.9×10^{7}	6.1×10^{7}

5.3 Rich Methane Flame Simulations

5.3.1 Neutral species

Graphs of major neutral species for a methane flame with equivalence ratio of 2.13 are shown in Figures 5.13–5.15. The experimental profiles are taken from a study conducted by Goodings *et al.* [32].

The O_2 and CH_4 profiles demonstrate good agreement with the experimental data. The major stable products, H_2, H_2O, and CO reach post flame concentrations that are close to the measured values. However, they reach these values at a position that is further downstream. They also appear earlier upstream compared to the experimental data. The experimental temperature profile found in Goodings *et al.* [32] paper had abrupt changes in the pre- and postflame regions. This temperature profile is smoothed to prevent numerical instabilities caused by the abrupt temperature changes. The smooth temperature profile is responsible for early appearance of these species in the flame. It is also responsible for these species reaching equilibrium

values further downstream.

This model predicts a CH_3 concentration that is a factor of two lower than the data from Goodings *et al.* [32]. This is because for rich flames, CH_3 is quickly depleted to produce C_2H_6. This same trend was observed in the rich flame simulations performed by Coffee *et al.* [2]. They reported a reduction in the CH_3 profile by a factor of three compared to the experimental data for a rich flame. However, the actual equivalence ratio used by Coffee *et al.* [2] was not documented.

The predicted value of C_2H_2 is also a factor of two lower than the experimental data. CH_3 is directly responsible for the production of C_2H_2, thereby causing the factor of two discrepancy in the data. These differences can be attributed to an incomplete understanding of the intermediate reactions responsible for the oxidation of CH_4.

5.3.2 Ionic species

The predicted and measured ionic species are in Figures 5.16–5.18. These profiles are for a rich flame (Φ=2.13) at atmospheric pressure. The experimental values are taken from Goodings *et al.* [32].

The model correctly predicts the H_3O^+ and $C_3H_3^+$ ions as the dominant ions. $C_3H_3^+$ and H_3O^+ are predicted to be of the same order of magnitude, which agrees with experimental data of Goodings *et al.* [32]. The concentration of $C_2H_3O^+$ relative to the concentrations of H_3O^+ and $C_3H_3^+$ is also in good agreement with the experimental data.

The model predicts the peak concentration of $C_3H_3^+$ and $C_2H_3O^+$ to be in the flame front followed by a rapid decrease in concentration. This is the accepted general

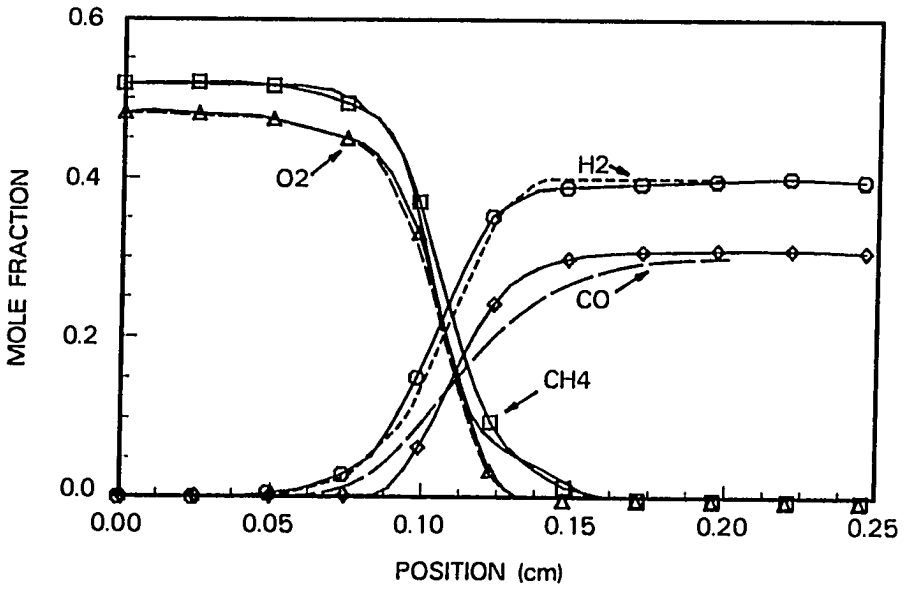

Figure 5.13: Predicted and experimental profiles for CH_4, O_2, H_2, and CO for a CH_4/O_2 flame (Φ=2.13). The experimental data are denoted by symbols [32]

trend for these two ions in flames. The peak concentration of H_3O^+ appears downstream of $C_3H_3^+$ and $C_2H_3O^+$ which is in agreement with the experimental data. This trend for H_3O^+ is caused by the reaction

$$H_3O^+ + e^- \rightarrow H_2O + H.$$

Van Tiggelen [66] reports that for rich methane flames , concentrations of CH_3^+ and CHO^+ are about one-tenth that of H_3O^+. Peeters *et al.* [65] report that concentrations of CH_3^+ and CHO^+ are a factor of 100 smaller than that of H_3O^+. Goodings *et al.* [32] show the ion concentration of CH_3^+ to be a factor of 400 smaller and the concentration of CHO^+ to be a factor of 600 smaller than H_3O^+. The predictions by this model show CH_3^+ and CHO^+ concentrations to be three orders of magnitude

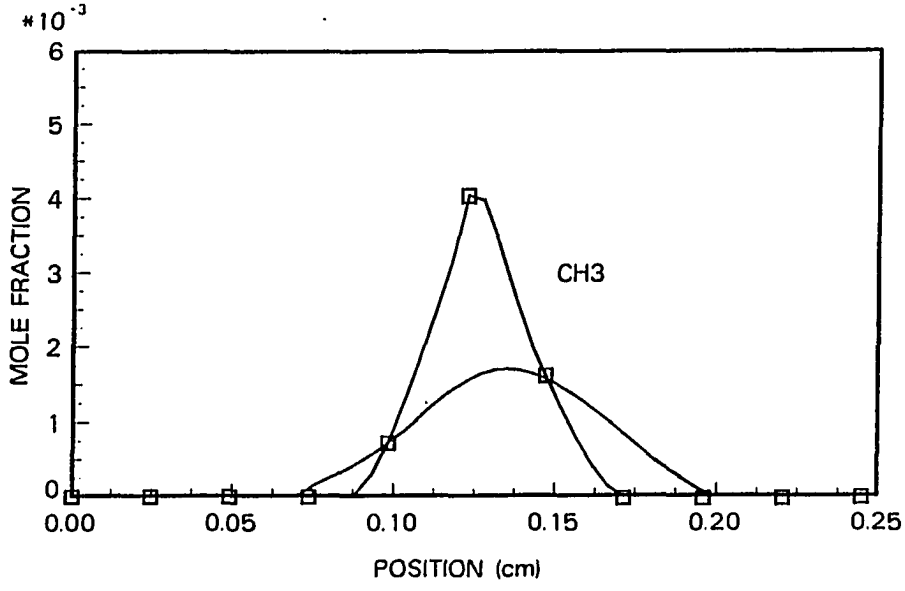

Figure 5.14: Predicted and experimental profile for CH_3 for a CH_4/O_2 flame (Φ=2.13). The experimental data are denoted by symbols [32]

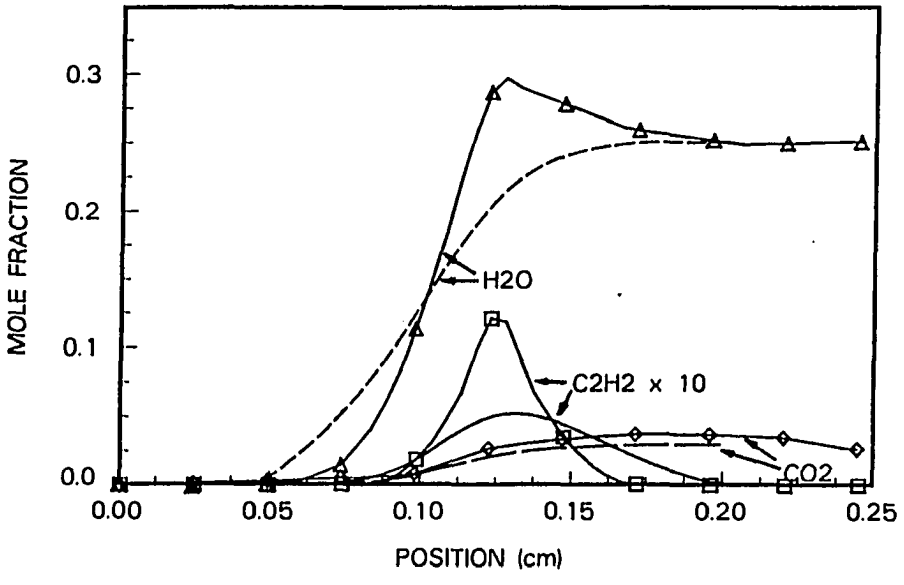

Figure 5.15: Predicted and experimental profiles for H_2O, C_2H_2 and CO_2 for a CH_4/O_2 flame (Φ=2.13). The experimental data are denoted by symbols [32]

smaller than the concentrations of H_3O^+. The lower predicted concentrations for these two ion can be traced back to the neutral species model. It produces a lower concentration of CH_3 and C_2H_2 by a factor of two. Since CH and CH_2 are derived from these two species, it can be assumed that it too is smaller than what might otherwise be expected. CH and CH_2 are precursors of CHO^+ and CH_3^+ which results in the lower concentration of these two ions.

The experimental profiles for CH_3^+ and CHO^+ show trends that are not in accord with accepted ideas on ions in flames. The experimental data shows the CH_3^+ ion to peak before the flame front with a slow decay that extends throughout the post–flame region. The experimental CHO^+ profile exhibits two peaks, one before and one after the flame front. These discrepancies may be the result of the expansion cooling in the sampling nozzle during the experiment.

5.4 Stoichiometric Hydrogen Flame Simulations

A hydrogen reaction mechanism is an underlying feature of the methane reaction mechanism in Table 3.1. This allows for studies to be performed on hydrogen flames seeded with methane.

It has been shown that hydrogen flames produce only minute quantities of ions when burned in air or oxygen [22, 31, 67]. These small concentrations are thought to arise from impurities. By seeding the hydrogen with small amounts of methane, ions are formed and effective activation energies for the ionic mechanism can be investigated.

A simulation to check the validity of the hydrogen mechanism is performed. The results of a stoichiometric hydrogen–air flame simulation at one atmosphere are

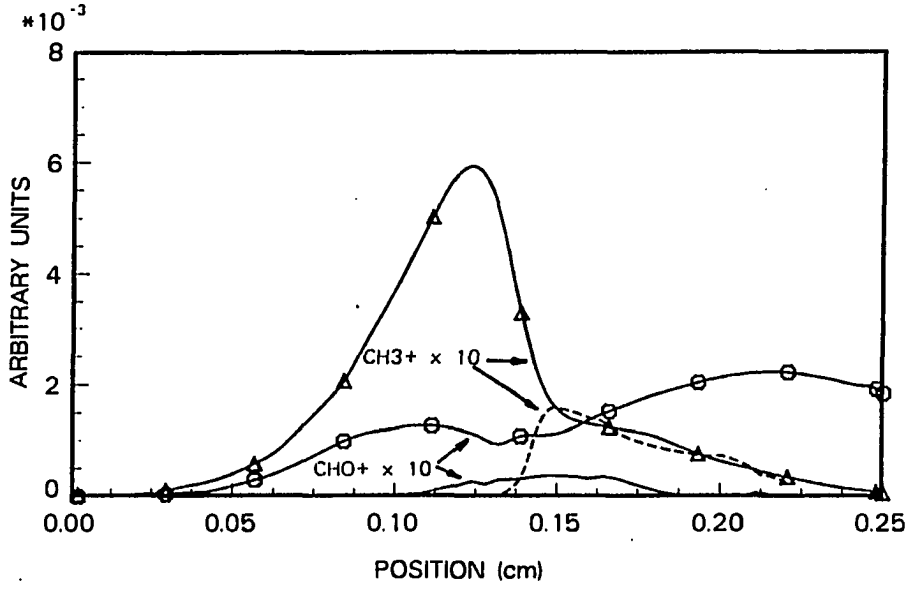

Figure 5.16: Predicted and experimental profiles for CH_3^+ and CHO^+ for a CH_4/O_2 flame (Φ=2.13). The experimental data are denoted by symbols [32]

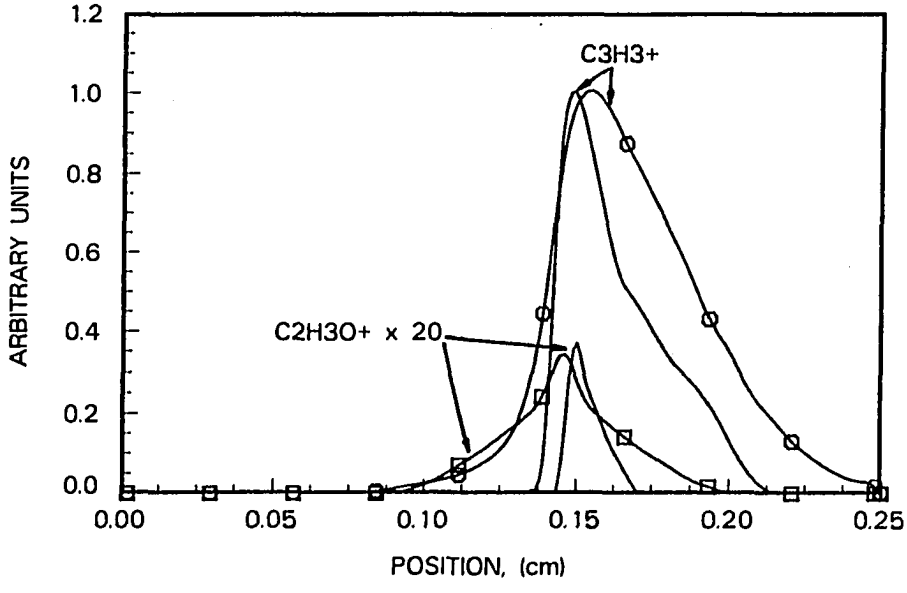

Figure 5.17: Predicted and experimental profiles for $C_3H_3^+$ and $C_2H_3O^+$ for a CH_4/O_2 flame (Φ=2.13). The experimental data are denoted by symbols [32]

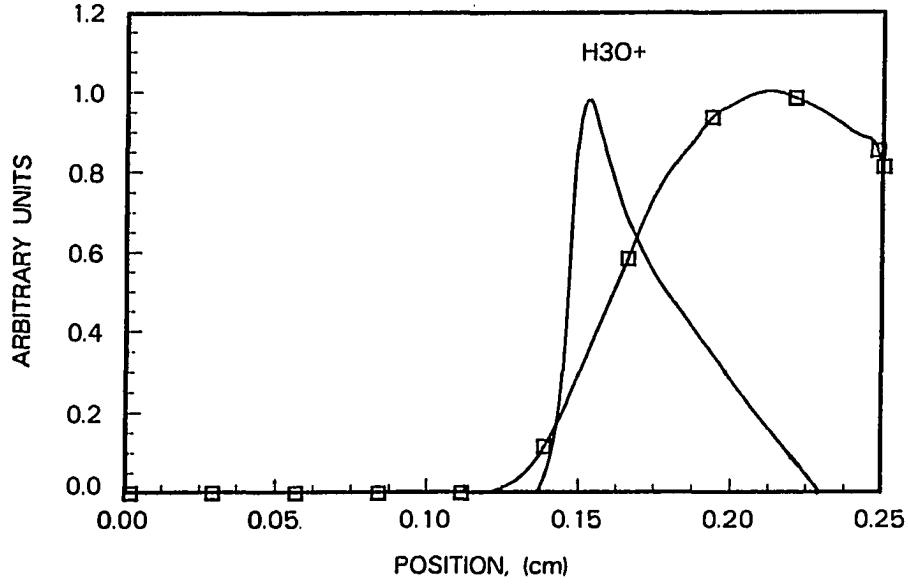

Figure 5.18: Predicted and experimental profiles for H_3O^+ for a CH_4/O_2 flame (Φ=2.13). The experimental data are denoted by symbols [32]

shown in Figures 5.19 and 5.20. Most resulting species concentration profiles are in excellent agreement with those by Warnatz [68]. The only discrepancy is the HO_2 profile which the present model overpredicts. This is thought to be the result of the omission of reactions which involve H_2O_2. The reactions involving this species are included in the mechanism used by Warnatz [68].

5.4.1 Hydrogen/methane flame simulations

The stoichiometric hydrogen flame is seeded with 1.8% methane. The major ion, H_3O^+, peaks just after the flame front and exhibits a slow decay in the post-flame region. It has an ion density of $1.0 \times 10^{11}/cm^3$. Peeters *et al.* [65] report a value of approximately $1.8 \times 10^{11}/cm^3$. The experimental profile also shows a slow decay in the

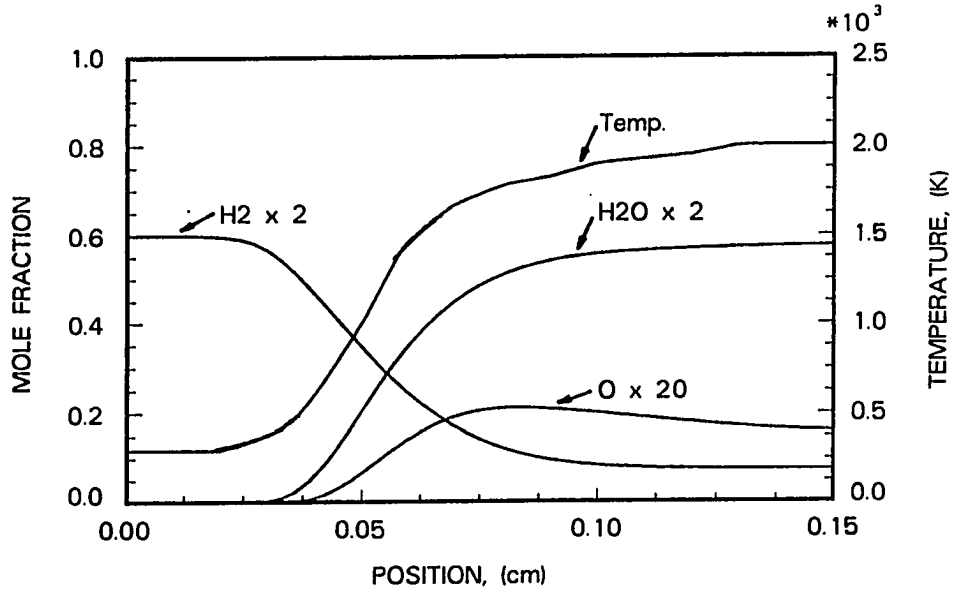

Figure 5.19: Predicted and profiles for H_2, H_2O and O for a H_2/air flame (Φ=1.00)

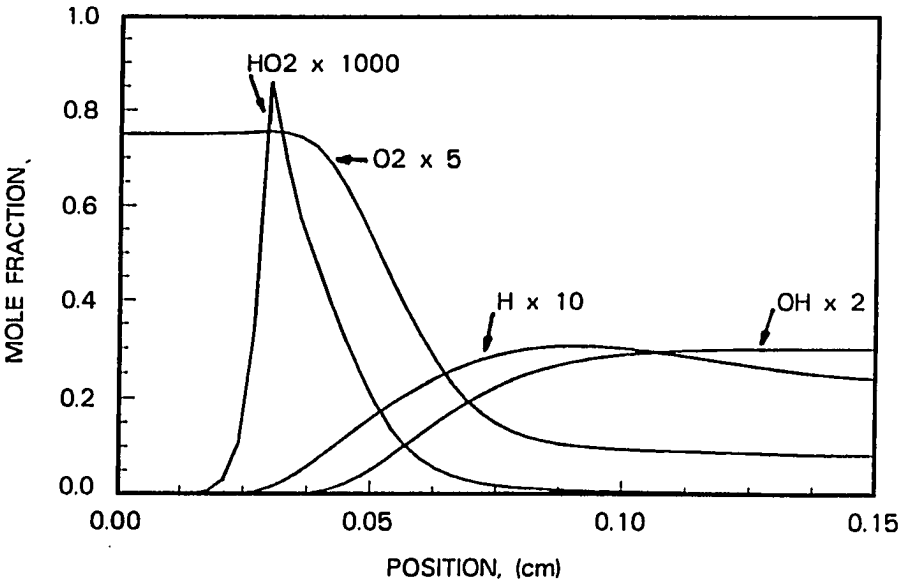

Figure 5.20: Predicted and profiles for HO_2, O_2, OH, and H for a H_2/air flame (Φ=1.00)

post–flame region.

The model predicts an ion density on the order of $10^9/cm^3$ for the $C_2H_3O^+$ ion. The model predicts all other ions to have ion densities lower than $10^3/cm^3$. The experimental results of Peeters *et al.* [65] document an ion density of $10^9/cm^3$ for $C_2H_3O^+$. The CHO^+, CH_3^+, and $C_3H_3^+$ ions do not appear in significant quantities in the flame and therefore are not reported by them.

In their experiments, Peeters *et al.* [65] measure a large concentration of CH_5O^+ in the flame. It is reported to have a ion density of $2.5x10^{10}/cm^3$. The reaction mechanism used in the present research does not take into account the formation of this ion which is usually not considered a major flame ion.

5.5 Predicted Effective Activation Energies, E_e

A steady state concentration of ions in a flame is reached when that rate of ion generation is equal to the rate that ions are removed by recombination. When an electric field is applied to the flame, ion removal is enhanced by the applied potential. As the potential is increased, ion removal by the electric field becomes dominant over ion removal by recombination. The current produced by the ion movement is the saturation current, j_s.

Since experimental temperature profiles are used in the simulations, it is a simple task to scale the temperature profile to a new final flame temperature. By varying the flame temperature and electric field strength, a saturation current can be found for each value of final flame temperature [57].

The plot of $\ln(j_s)$ vs. $1/T_f$, where T_f is the final flame temperature, yields a straight line. The slope of this line is equal to the effective activation energy for

the ionic mechanism [8, 36]. This activation energy can be used to yield information concerning the mechanisms involved in ion formation.

5.5.1 E_e for the lean methane flame

The saturation currents for a lean methane flame are shown in Table 5.3. The saturation current is calculated for three different final flame temperatures: 1700, 1900, and 2200 K. The effective activation energy is equal to the slope of the line for $\ln(j_s)$ vs. $1/T_f$. The effective activation energy for the lean flame is in Table 5.3.

Table 5.3: Predicted effective activation energy for a lean methane flame

T_f (K)	j_s (μA/cm^2)	$E_{e\ pred.}$ (kcal/mole)
2200	5.07	
1900	0.29	41.36
1700	0.02	

There is a lack of experimental saturation currents and effective activation energies for the lean (Φ=0.2) methane flame simulated in this research. Experimental effective activation energies reported by several researchers [8, 36, 37, 65] have been shown to range in value from 37.5$\pm$2 to 73.0 kcal/mole for slightly lean to slightly rich flames. The predicted effective activation energy in Table 5.3 falls within the range of these upper and lower values.

The next step is to find the relationship between the predicted effective activation energy and the reaction mechanism used in this work. The activation energies, E_a, used in the ionic reaction mechanism are compared to the predicted effective activation energy, E_e. Any reaction that has an activation energy, E_a, with the same

magnitude as the predicted effective activation energy, E_e, is subjected to a sensitivity analysis. The activation energy, E_a, for a suspected reaction is divided by two and a new predicted effective activation energy, E'_e, is calculated. This is done for each of the suspected reactions. The reaction that produces an effective activation energy, E'_e, equal to its original activation energy divided by two, $E_a/2$, is thought to be the rate limiting reaction responsible for controlling the ionization of the flame.

For the lean flame, the reaction

$$C_2H_3O^+ + H_2 \rightarrow H_3O^+ + C_2H_2$$

is responsible for the predicted effective activation energy. Upon tracing the path followed by the ions, it is found that the primary charge recombination mechanism is

$$H_3O^+ + e^- \rightarrow H + H_2O.$$

A schematic of the ionic reaction mechanism is shown in Figure 5.21. The movement of ions in the lean flame are denoted in Figure 5.21 by the oversized arrows. This implies that

$$C_2H_3O^+ + H_2 \rightarrow H_3O^+ + C_2H_2$$

is the rate limiting reaction in the ionic reaction mechanism.

5.5.2 E_e for the stoichiometric methane flame

The final flame temperature, corresponding saturation current, and predicted effective activation energy for the stoichiometric flame are in Table 5.4. The experimental effective activation energy determined by Lawton and Weinberg [8, 36] is included in the table. Lawton and Weinberg [8, 36] did not document the saturation

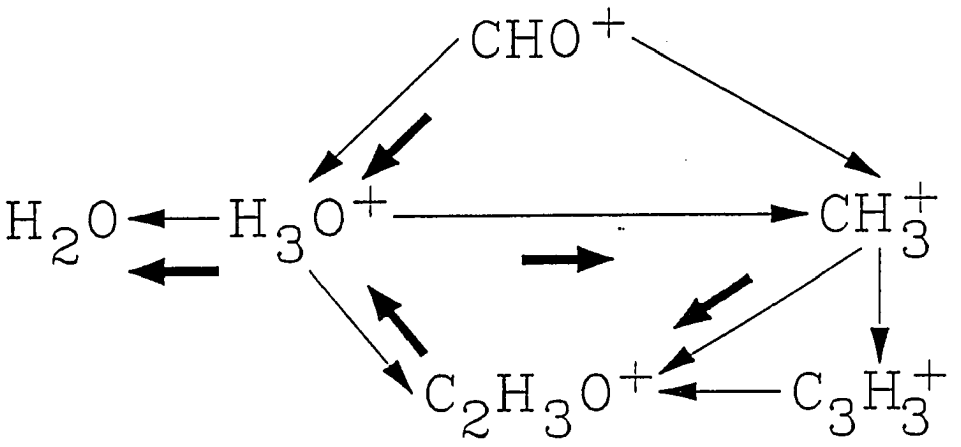

Figure 5.21: Predicted ion movement in a methane flame, Φ=0.21

currents or final flame temperatures that produced this result. This does not allow for a direct comparison between the predicted and experimental values of saturation currents. However, the predicted effective activation energy compares well to that measured experimentally. The values are within 1 kcal/mole of each other.

It is necessary to determine which of the reactions in the ionic model is responsible for the predicted effective activation energy. Further investigation into the path taken by the ions in the ionic mechanism is conducted. The oversized arrows in Figure 5.22 indicate the pathway followed by the ions. This confirms the belief that

$$H_3O^+ + e^- \rightarrow H + H_2O$$

is the primary charge recombination mechanism in flames [36]. It also implies that

Table 5.4: Experimental [8, 36] and predicted effective activation energy for a stoichiometric methane flame

T_f (K)	j_s (μA/cm^2)	$E_{e\ pred.}$ (kcal/mole)	$E_{e\ exp}$ (kcal/mole)
2200	36.10		
1900	1.31	46.81	46.00
1700	0.07		

the reaction,

$$C_2H_3O^+ + H_2 \rightarrow H_3O^+ + C_2H_2$$

is the rate limiting reaction in the mechanism. The effective activation energy for this reaction is within 11% of the predicted value.

To be certain that this is indeed the rate limiting reaction, the effective activation energy for the reaction is decreased by a factor of 2 to 23 kcal/mole. Another series of simulations are run and the saturation currents and effective activation energy again are calculated. The new effective activation energy, based on the new saturation currents, is equal to 21.96 kcal/mole. In agreement to within 5% of the altered value of 23 kcal/mole. Therefore, it is concluded that the reaction,

$$C_2H_3O^+ + H_2 \rightarrow H_3O^+ + C_2H_2,$$

is the rate limiting reaction in the ionic model.

5.5.3 E_e for the rich methane flame

The effective activation energy and saturation currents for the rich flame simulations are in Table 5.5. Comparing the saturation currents in Tables 5.3–5.5 shows an increase in the saturation current with equivalence ratio until it reaches unity. As

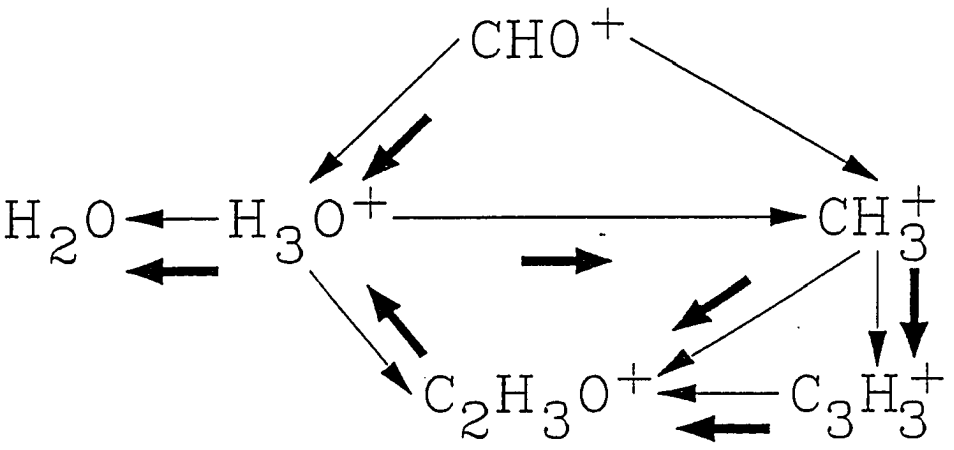

Figure 5.22: Predicted ion movement in a methane flame, Φ=1.00

the flame is made rich, the saturation current then decreases in value. This trend, shown in Figure 5.23, is supported by experimental observations made by Peeters *et al.* [65] for other hydrocarbon flames. This behavior is due to the maximum rate of ion generation that occurs in the stoichiometric flame.

There is a lack of experimentally determined saturation currents for rich methane flames. This does not allow for a comparison to be made between predicted and experimental data.

The predicted effective activation energy for the rich flame is 42.47 kcal/mole. Again, it is necessary to determine which of the reactions in the ionic model is responsible for the predicted effective activation energy. A sensitivity analysis is

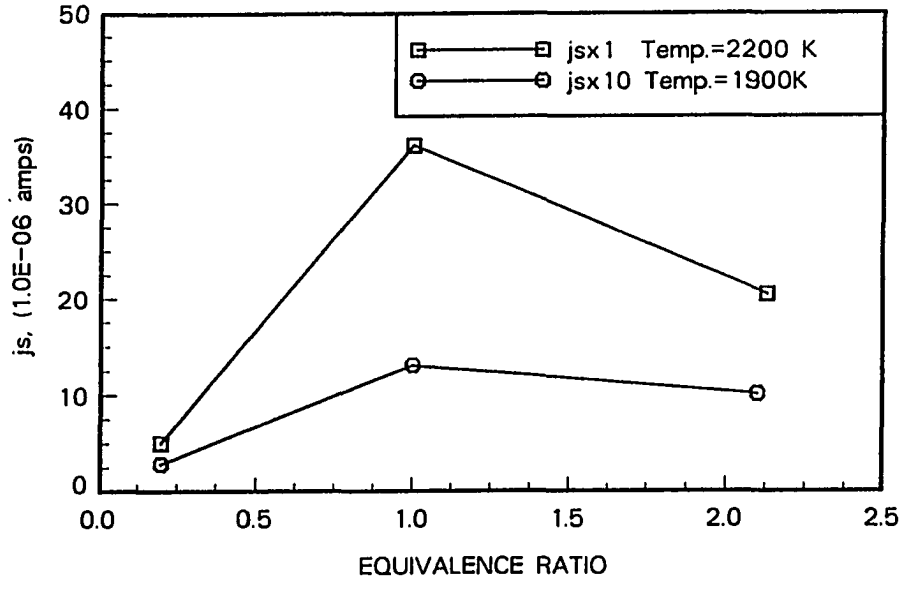

Figure 5.23: Predicted saturation currents as a function of equivalence ratio

performed on the ionic reaction mechanism. The sensitivity analysis used in the rich flame is analogous to the one used in the lean and stoichiometric cases. The results show that the reaction,

$$C_2H_3O^+ + H_2 \rightarrow H_3O^+ + C_2H_2,$$

is the rate limiting reaction in the rich flame simulations also.

The path followed by the ions in the rich flame is indicated by the oversized arrows in Figure 5.24. It is reaffirmed that

$$H_3O^+ + e^- \rightarrow H + H_2O$$

is the primary reaction for charge recombination in the mechanism [36].

Table 5.5: Predicted effective activation energy for a rich methane flame

T_f (K)	j_s (μA/cm^2)	$E_{e\ pred.}$ (kcal/mole)
2200	20.50	
1900	1.01	42.47
1700	0.06	

5.5.4 E_e for the stoichiometric hydrogen/methane flame

Lawton and Weinberg [8, 36] measured saturation currents (Table 5.6) for a stoichiometric hydrogen flame seeded with 1% methane. The methane mechanism used in this research is shown to accurately simulate a hydrogen flame. The simulation results in Table 5.6 represent the predicted values for a stoichiometric hydrogen/methane flame.

The difference between the experimental and predicted saturation currents range from a factor of two at 1555 K to a factor of four at 1456 K. The saturation currents are a function of the total ion current produced by the flame. The experimental and predicted saturation currents are in good agreement considering the ionic reaction mechanism predicted a total ion density that was a factor of 1.8 lower than the experimental data.

The predicted effective activation energy is 51% lower than the measured value. However, it does fall into the range of values predicted by the methane flame simulations. A sensitivity analysis is conducted since there is good agreement between the predicted and experimental saturation currents.

It is reasonable to assume that the reactions controlling the ionic processes in

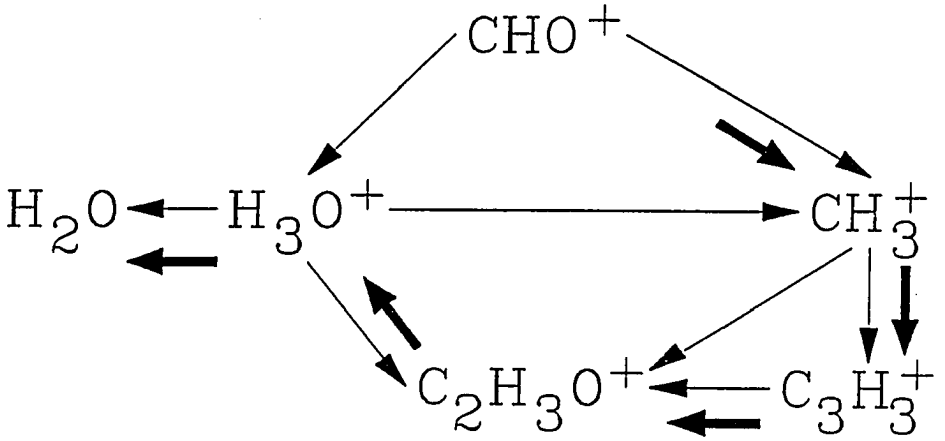

Figure 5.24: Predicted ion movement in a methane flame, Φ=2.13

methane flames would be the same as those controlling the hydrogen/methane flame. This assumption turns out to be valid since the rate limiting reaction is the reaction,

$$C_2H_3O^+ + H_2 - H_3O^+ + C_2H_2.$$

The mechanism controlling ion depletion is also the same as it was for the methane flame:

$$H_3O^+ + e^- \rightarrow H + H_2O.$$

The path followed by the ions for this hydrogen/methane flame is identical to the path followed by the stoichiometric methane flame in Figure 5.22.

Table 5.6: Experimental [8, 36] and predicted effective activation energy for a stoichiometric hydrogen/methane flame

T_f (K)	$j_{s\ pred}$ (μA)	$E_{e\ pred.}$ (kcal/mole)	$j_{s\ exp}$ (μA)	$E_{e\ exp}$ (kcal/mole)
1555	0.110		0.23	
1530	0.064		0.18	
1511	0.049	42.60	0.14	28.10
1490	0.030		0.10	
1456	0.017		0.07	

6. CONCLUSIONS

A simple ionic reaction mechanism is proposed that accurately predicts the general features of ions in lean to stoichiometric methane flames. The proposed reaction mechanism provides a means for the production and recombination of the major ions thought to be found in methane flames. The rich flame simulations show the ionic mechanism does not produce enough CHO^+ and CH_3^+ ions. This is attributed to the neutral species reaction mechanism and the uncertainties associated with the details of the intermediate reactions in the oxidation of CH_4.

Using this ionic reaction mechanism, the saturation currents for a lean, stoichiometric, and rich methane flame are calculated. Some literature exists that contains experimental saturation currents. However, rarely are the saturation currents reported as functions of temperature. This deficiency does not allow for a direct comparison between the experimental and the predicted saturation currents. The general trend of saturation current vs. equivalence ratio is predicted in this work.

The saturation currents as a function of final flame temperature is used to determine the effective activation energies for the ionization process. The predicted values range from 41.36 kcal/mole for the lean flame to 46.81 kcal/mole for the stoichiometric flame. These values fall into the range of values reported in the literature for methane flames.

The predicted effective activation energies are used to determine the rate limiting reaction in the ionic reaction mechanism. It is determined that effective activation energies predicted by the simulations corresponded to the reaction,

$$C_2H_3O^+ + H_2 \rightarrow H_3O^+ + C_2H_2,$$

for all equivalence ratios. The tracing of ions through the ionic reaction mechanism verifies that this reaction is indeed the rate limiting reaction. The movement of ions through the ionic reaction mechanism for the lean, stoichiometric, and rich methane flames are shown in Figures 6.1-6.3. In all cases, the primary mechanism for deactivation is the same. The dissociative recombination reaction,

$$H_3O^+ + e^- \rightarrow H + H_2O,$$

is the primary outlet for the ions.

A stoichiometric hydrogen flame seeded with small concentrations of methane is also investigated in this work. The same ionic reaction mechanism is used for these simulations that was used in the methane flame simulations.

The major ion predicted by the model is H_3O^+. This value is in good agreement with the experimental data. However, the experimental data show CH_5O^+ to be the second largest ion, in concentration, present in the flame. This ion is not included in the ionic reaction mechanism.

The saturation currents predicted for the hydrogen/methane flame are in good agreement with experimental values. The differences range from a factor of two to a factor of four.

The rate limiting reaction for the hydrogen/methane flame is

$$C_2H_3O^+ + H_2 \rightarrow H_3O^+ + C_2H_2.$$

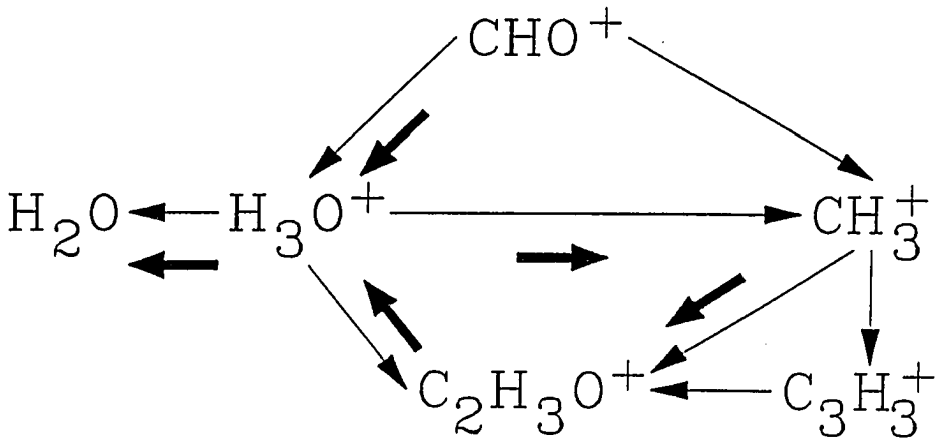

Figure 6.1: Predicted ion movement in a methane flame, Φ=0.21

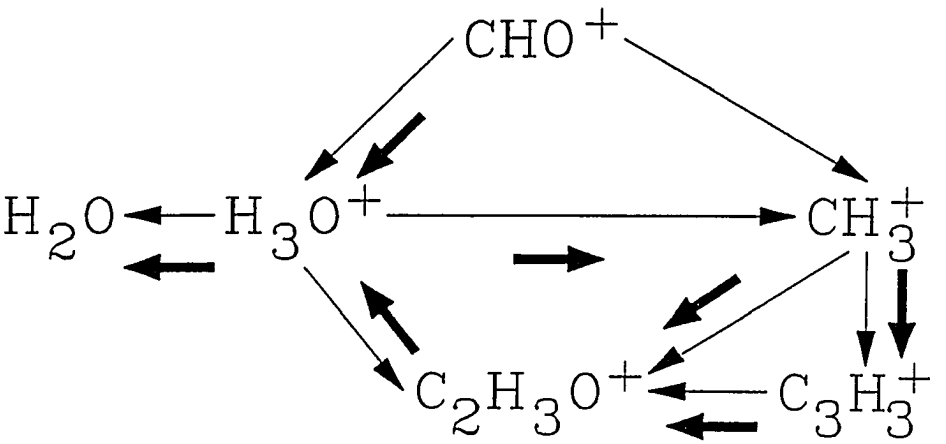

Figure 6.2: Predicted ion movement in a methane flame, Φ=1.00

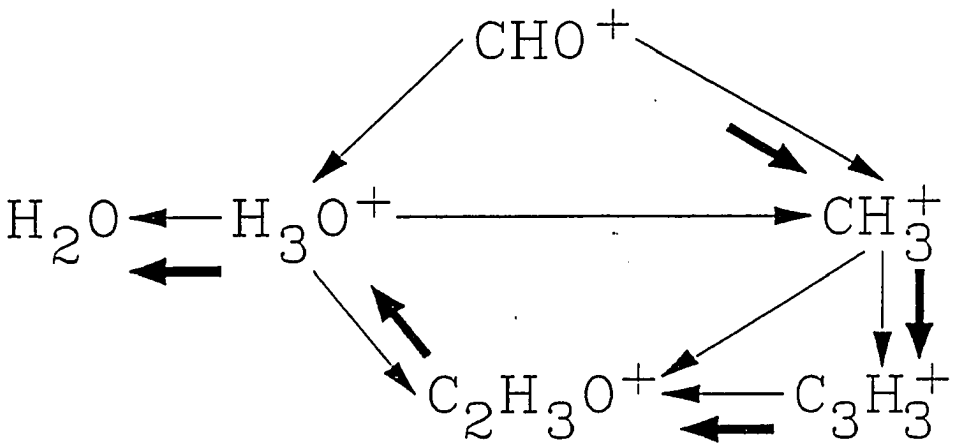

Figure 6.3: Predicted ion movement in a methane flame, Φ=2.13

The ion path for this flame is the same pathway taken by the ions in a stoichiometric methane flame (Figure 6.2). The reaction,

$$H_3O^+ + e^- \rightarrow H + H_2O,$$

is again the primary reaction in the deactivation of the ions.

It is recommended that the variation of saturation current with final flame temperature be experimentally carried out and documented extensively for a methane flame. This will allow for a better comparison between experimental and predicted values.

A study into the details of the intermediate reactions in the oxidation of CH_4 is also suggested. Once these intermediate reactions are known, an improvement in the

prediction of ions in rich flames will result.

An experimental investigation into the ions formed in a hydrogen/methane flame is needed to verify the appearance of CH_5O^+. It is possible that the experimental observation of this ion by researchers has been mistaken for the CHO^+ ion.

BIBLIOGRAPHY

[1] Bechtel, J.H., Blint, Richard J., Dasch, Cameron J., and Weinberger, Doreen A. "Atmospheric Pressure Premixed Hydrocarbon–Air Flames: Theory and Experiment," *Combustion and Flame*, 42 (1981): 197-213.

[2] Coffee, Terence P. "Kinetic Mechanism for Premixed, Laminar, Steady State Methane/Air Flames," *Combustion and Flame*, 55 (1984): 161-170.

[3] Smoot, Douglas L., Hecker, William C., and Williams, Gerald A. "Prediction of Propagating Methane–Air Flames," *Combustion and Flame*, 26 (1976): 323-342.

[4] Paczko, G., Lefdal, P.M., and Peters, N. "Reduced Reaction Schemes for Methane, Methanol and Propane Flames," *Twenty-first Symposium (International) on Combustion/The Combustion Institute*, 21 (1986): 739-748.

[5] Tsatsaronis, Georgios "Prediction of Propagating Laminar Flames in Methane, Oxygen, Nitrogen Mixtures," *Combustion and Flame*, 33 (1978): 217-239.

[6] Warnatz, J. "The Structure of Laminar Alkane-, Alkene-, and Acetylene Flames," *Eighteenth Symposium (International) on Combustion/The Combustion Institute*, 18 (1981): 369-384.

[7] Warnatz, J. "Rate Coefficients in the C/H/O System," In *Combustion Chemistry*. W.C. Gardiner, Jr., ed. Springer-Verlag, New York, 1984, 197-360.

[8] Lawton, F. and Weinburg, F.J. "Maximum Ion Currents From Flames and the Maximum Practical Effects of Applied Electrical Fields," *Proceedings of the Royal Society A.*, 277 (1964): 468-497.

[9] Calcote, H.F., Kurzius, S.C., and Miller, W.J. "Negative and Secondary Ion Formation in Low–Pressure Flames," *Tenth Symposium (International) on Combustion/The Combustion Institute*, 10 (1965): 605-619.

[10] Peeters, J. and Van Tiggelen, A. "Experimental Determination of the Rate of the Chemiionization Process," *Twelfth Symposium (International) on Combustion/The Combustion Institute*, 12 (1968): 437-446.

[11] Oran, Elaine S. and Boris, Jay P. "Numerical Simulation of Reactive Flow," Elsevier, New York, 1987.

[12] Eraslan, Ahmet N., and Brown, Robert C. "A Simple Iterative Procedure for Reducing Stiffness and Computer Memory in Reactive Flow Problems," *Computer Methods in Applied Mechanics and Engineering*, 64 (1987): 61-77.

[13] Thompson, J.J. and Thompson, G.P. *Conductivity of Electricity Through Gases* Vol. 1, 3^{rd} edition. Cambridge University Press, Cambridge, 1928.

[14] Erman, G. *Ann.*, Vol. 11, 1802.

[15] Arrhenius, S. *Ann. Physik*, Vol. 42, 1891.

[16] Thompson, J.J., *Rept. Brit. Assoc. for Adv. of Science*, 8 (1910): 510.

[17] Tanford, C. and Pease, R.N. "Equilibrium Atom and Free Radical Concentrations in Carbon Monoxide Flames and Correlation with Burning Velocity ," *Journal of Chemical Physics*, 15 (1947): 431-433.

[18] Calcote, H.F. "Electrical Properties of Flames," Dissertation, Princeton University, (1947).

[19] Littlewood, A.B. *Gas Chromatography* Academic Press, London, 1962.

[20] Sugden, T.M. "Elementary Combustion Reactions. Charged Species," *Tenth Symposium (International) on Combustion/The Combustion Institute*, 10 (1965): 539-544.

[21] Desty, D.H., Geach, C.J., and Goldup, A. "An Examination of the Flame Ionization Detector Using a Diffusion Dilution Apparatus," *Third Symposium (International) on Gas Chromatography*, 3 (1960): 46-64.

[22] Bulewicz, E.M., and Padley, P.J. "A Cyclotron Resonance Study of Ionization in Low–Pressure Flames," *Ninth Symposium (International) on Combustion/The Combustion Institute*, 9 (1963): 638-646.

[23] Calcote, H.F. "Ion Production and Recombination in Flames," *Eighth Symposium (International) on Combustion/The Combustion Institute*, 8 (1960): 184-199.

[24] Fontijn, A. and Baughman, G.L. "Chemi-Ionization in the Room Temperature Reaction of Oxygen Atom with Acetylene," *Journal of Chemical Physics*, 38 (1963): 1784-1785.

[25] Fontijn, A., Miller, W.J., and Hogan, J.M. "Chemi-Ionization and Chemiluminescence in the Reaction of Atomic Oxygen with C_2H_2, C_2D_2, and C_2H_4," *Tenth Symposium (International) on Combustion/The Combustion Institute*, 10 (1965): 545-560.

[26] Miller, W.J. "Low-Pressure Flame Composition and the Origin of $C_3H_3^+$," *Eleventh Symposium (International) on Combustion/The Combustion Institute*, 11 (1967): 311-319.

[27] Glass, J.P., Kistiakowsky, G.B., Michael, J.V., and Nike, H. "Mechanism of the Acetylene–Oxygen Reaction in Shock Waves," *Journal of Chemical Physics*, 42 (1965): 608-621.

[28] Bulewicz, E.M. "Comments on Low-Pressure Flame Composition and the Origin of $C_3H_3^+$," *Eleventh Symposium (International) on Combustion/The Combustion Institute*, 11 (1967): 319-320.

[29] Warnatz, J. "Gas–Phase Chemiluminescence and Chemi-Ionization," A. Fontijn, ed. Elsevier Science Publishers, B.V., 1985.

[30] Eraslan, Ahmet N. and Brown, Robert C. "Chemiionization and Ion-Molecule Reactions in Fuel-Rich Acetylene Flames," *Combustion and Flame*, 74 (1988): 19-37.

[31] Green, J.A. and Sugden, T.M. "Some Observations on the Mechanism if Ionization in Flames Containing Hydrocarbons," *Ninth Symposium (International) on Combustion/The Combustion Institute*, 9 (1963): 607-621.

[32] Goodings, J.M., Bohme, K.D., and Sugden, T.M. "Positive Ion Probe of Methane-Oxygen Combustion," *Sixteenth Symposium (International) on Combustion/The Combustion Institute*, 16 (1977): 891-902.

[33] Miller, William J. *Ionization in Combustion Processes in Oxidation and Combustion Reviews* Elsevier Publishing Company, Amsterdam, 1968.

[34] Brown, Robert C. and Eraslan, Ahmet N. "Simulation of Ionic Structure in Lean and Close-to-Stoichiometric Acetylene Flames," *Combustion and Flame*, 73 (1988): 1-21.

[35] Goodings, J.M., Bohme, K.D., Chun-Wai, NG. "Detailed Ion Chemistry in Methane-Oxygen Flames. I. Positive Ions," *Combustion and Flame*, 36 (1979): 27-43.

[36] Lawton, J., and Weinberg, F. "Electrical Aspects of Combustion," Clarendon Press, Oxford, London, 1969.

[37] Bertrand, C., Dussart, B., and Van Tiggelen, P.J. "Use of Electric Fields to Measure Burning Velocities," *Seventeenth Symposium (International) on Combustion/The Combustion Institute*, 17 (1978): 967-973.

[38] Dixon–Lewis, G. in *First Specialist Meeting (International) on Combustion/The Combustion Institute*, France, 284-289.

[39] Dixon–Lewis, G. "Kinetic Mechanisms, Structure, and Properties of Premixed Flames in Hydrogen-Oxygen-Nitrogen Mixtures," *Phil. Trans.Roy. Soc. (London)*, A292 (1979): 45-99.

[40] Dean, A.M., Johnson, R.L., and Steiner, D.C. "Shock-Tube Studies of Formaldehyde Oxidation," *Combustion and Flame*, 37 (1980): 41-62.

[41] Dean, A.M. and Johnson, R.L. "Shock-Tube Studies of the $N_2O/CH_4/CO/Ar$ and $N_2/C_2H_6/CO/Ar$ Systems," *Combustion and Flame*, 37 (1980): 109-123.

[42] Gelinas, R.J. *Science Applications*. Preprint No. SAI/PL/C297,1979.

[43] Luther, K. and Troe, J. "Weak Collision Effects in Dissociative Reactions at High Temperatures," *Seventeenth Symposium (International) on Combustion/The Combustion Institute*, 17 (1979): 535-542.

[44] Ay, J., Ong, R.S.B., and Sichel, H. "A Simple Mathematical Model for Ionization in Flames," *Combustion Science and Technology*, 11 (1975): 19-28.

[45] Eraslan, Ahmet Nedim "Prediction of Ionic Structure in Hydrocarbon Flames," Dissertation, Iowa State University, (1987).

[46] Su, T. and Bowers, M.T. "Theory of Ion–Polar Molecule Collisions. Comparison with Experimental Charge Transfer Reactions of Rare Gas Ions to Geometric Isomers of Difluorobenzene and Dichloroethylene," *Journal of Chemical Physics*, 58 (1973): 3027-3037.

[47] Su, T. and Bowers, M.T. "Ion–Polar Molecule Collisions. The Effect of Ion Size on Ion–Polar Molecule Rate Constants; The Parameterization of the Average–Dipole–Orientation Theory," *International Journal of Mass Spectroscopy in Ion Physics*, 12 (1973): 347-356.

[48] Su, T., Su, C.F.E. and Bowers, M.T. "Ion–Polar Molecule Collisions. Conservation of Angular Momentum in the Average Dipole Orientation Theory. The AADO Theory," *Journal of Chemical Physics*, 69 (1978): 2243-2250.

[49] Stull, D.R. and Prophet, H. *JANAF Thermochemical Tables*. $2^{\underline{nd}}$ edition. National Standard Reference Data Series. U.S. National Bureau of Standards, Washington, D.C., 1971.

[50] Anicich, V.G., Huntress, Jr., W.T. and McEwan, M.J. *Jet Propulsion Laboratory Report*, California Technical Institute, 1985.

[51] Delfau, J.L. and Barassin, A. "The Positive Ion Chemistry in the Post–Combustion Zone of Sooting Premixed Acetylene Low Pressure Flat Flames," *Eighteenth Symposium (International) on Combustion/The Combustion Institute*, 18 (1980): 443-450.

[52] Spalding, D.B. and Stephenson, P.L. "Laminar Flame Propagation in Hydrogen+Bromine Mixtures," *Proceedings of the Royal Society A.*, 324 (1971): 315-337.

[53] Warnatz, J. "Calculation of the Structure of Laminar Flat Flames I: Flame Velocity of Freely Propagating Ozone Decomposition Flames," *Ber. Bunsenges. Physical Chemistry*, 82 (1978): 193-200.

[54] Hunter, S. R. and Christophorou, L. G. "Electron Motion in Low– and High–Pressure Gases," *Electron-Molecule Interactions and Their Applications*. L.G. Christophorou ed. American Press, New York, 1984, 89-220.

[55] Hindmarsh, A.C. "ODEPACK, A Systematized Collection of ODE Solvers," In *Scientific Computing*. R.S. Stepleman ed. North-Holland, Amsterdam, 1983.

[56] Goyal, G., Paul, P.J., Mukunda, H.S., and Deshpande, S.M. "Time Dependent Operator–split and Unsplit Schemes for One Dimensional Premixed Flames," *Combustion Science and Technology*, 60 (1988): 167-189.

[57] Pedersen, Timothy W. "Prediction of Saturation Currents in Methane Flames," Thesis, Iowa State University, (1990).

[58] Smooke, M.D., Miller, J.A., and Kee, R.J. "On the Use of Adaptive Grids in Numerically Calculating Adiabatic Flame Speeds." In *Numerical Methods in Laminar Flame Propagation.* N. Peters and J. Warnatz eds. Notes on Numerical Fluid Mechanics, Volume 6. Hayden and Son, Philadelphia, 1982.

[59] Dwyer, H.A., and Sanders, B.R. "Numerical Modelling of Unsteady Flame Propagation," *Acta Astronautica*, 5 (1978): 1171-1184.

[60] Eraslan, A.N. and Brown, R.C. "PROP: A Collection of Efficient FORTRAN Subroutines for Calculating Gas Mixture Properties." *Engineering Research Institute Technical Report*, Iowa State University, 1987.

[61] Peeters, Jozef and Mahnen, Gilbert "Reaction Mechanisms and Rate Constants of Elementary Steps in Methane–Oxygen Flames," *Fourteenth Symposium (International) on Combustion/The Combustion Institute*, 14 (1972): 133-146.

[62] Olsson, Jim, O. and Andersson, Lars, L. "Sensitivity Analysis Based on an Efficient Brute–Force Method, Applied to an Experimental CH_4/O_2 Premixed Laminar Flame," *Combustion and Flame*, 67 (1987): 99-109.

[63] Westbrook, C.K. and Dryer, F.L. "Chemical Kinetics and Modeling of Combustion Processes," *Eighteenth Symposium (International) on Combustion/The Combustion Institute*, 18 (1980): 749-767.

[64] Calcote, H.F. in "Ion–Molecule Reactions," Plenum Press, New York, 1972.

[65] Peeters, J., Vinkier, C., and Van Tiggelen, A. "Formation and Behavior of Chemi–Ions in Flames," *Oxidation and Combustion Reviews*, 4 (1969): 93-132.

[66] Van Tiggelen, A. in "Ionization in High Temperature gases," Academic Press, London and New York, 1963.

[67] Calcote, H.F. "Mechanisms for the Formation of Ions in Flames," *Combustion and Flame*, 1 (1957): 385-403.

[68] Warnatz, J. "Concentration–, Pressure–, and Temperature–Dependence of the Flame Velocity in Hydrogen–Oxygen–Nitrogen Mixtures," *Combustion Science and Technology*, 26 (1981): 203-213.

[69] Hirschfelder, J.O., Curtiss, C.F. and Bird, R.B. *Molecular Theory of Gases and Liquids*. $2^{\underline{nd}}$ edition. John Wiley and Sons, Inc., New York, 1964.

[70] Kee, R.J., Warnatz, J., and Miller, J.A. National Standard Reference Data Series. U.S. National Bureau of "A FORTRAN Computer Code Package for the Evaluation of Gas-Phase Viscosities, Conductivities, and Diffusion Coefficients." Sandia Report Number: SAND83-82009, 1983.

APPENDIX A. SHOOTING METHOD FOR SOLVING POISSON'S EQUATION

The methodology for a general second-order boundary-value problem of the form

$$\frac{dy}{dx} = f(x, y, y') \quad y(0) = y_0 \quad y(L) = y_L \tag{6.1}$$

is summarized as follows:

1. Using physical intuition choose approximate values for the initial slope $\frac{dy}{dx} = a$. Let them be a_1 and a_2.

2. Solve the boundary-value problem twice, as an initial-value problem using a_1 and a_2 as initial conditions along with $y(0) = y_0$. Call the solutions y_1 and y_2 at $x = L$.

3. Calculate the next approximation to the slope at $x = 0$ with

$$a_{i+1} = a_{i-1} + (a_i - a_{i-1}) \frac{y_{x=L} - y_{x=L}(a_{i-1})}{y_{x=L}(a_i) - y_{x=L}(a_{i-1})} \tag{6.2}$$

   for $i = 1, 2, \ldots$

4. Repeat steps 2 and 3 until a prescribed error for y_L is attained.

APPENDIX B. CALCULATION OF TRANSPORT PROPERTIES

The equations for the estimation of transport properties are borrowed from Hirschfelder *et al.* [69]. Other data are taken from Kee *et al.* [70].

The thermal conductivity of a pure gas is given by

$$\lambda_1 = 1989.1 \times 10^{-7} \frac{\left[\frac{T}{M}\right]^{\frac{1}{2}}}{\sigma^2 \Omega^{(2,2)*}(T^*)} \tag{6.3}$$

in the first approximation.

$T^* = \frac{T}{\frac{\epsilon}{k}}$ is the reduced temperature and $\Omega^{(2,2)*}$ is the collision integral calculated at the reduced temperature.

The Eucken equation corrects this for a polyatomic gas

$$\lambda_{1,poly} = \lambda_1 \left(\frac{20C_v + 45R}{75R}\right). \tag{6.4}$$

A first approximation to the thermal conductivity for a binary mixture is

$$\lambda_{(i,j)_1} = 1989.1 \times 10^{-7} \frac{\left[\frac{T(M_i + M_j)}{2M_iM_j}\right]^{\frac{1}{2}}}{\sigma_{i,j}^2 \Omega_{i,j}^{(2,2)*}(T_{i,j}^*)}. \tag{6.5}$$

A second approximation to the self diffusion coefficient of a gas is

$$D_{(i,i)_2} = D_{(i,i)_1} \cdot f_{D_{i,i}}^2 \tag{6.6}$$

where

$$D_{i,i_1} = 0.002628 \frac{\left[\frac{T^3}{M_i}\right]^{\frac{1}{2}}}{P\sigma_i^2 \Omega^{(1,1)*}(T^*)}, \tag{6.7}$$

and

$$f_{D_{i,i}}^2 = \frac{1}{1-\Delta}. \tag{6.8}$$

The expression for Δ is defined as

$$\Delta = \frac{(6c^*(T_i^*) - 5)^2}{(16A^*(T_i^*) - 12B^*(T_i^*) + 55)}, \tag{6.9}$$

where

$$A^*(T_i^*) = \frac{\Omega^{(2,2)*}(T_i^*)}{\Omega^{(1,1)*}(T_i^*)}, \tag{6.10}$$

$$B^*(T_i^*) = \frac{5\Omega^{(1,2)*}(T_i^*) - 4\Omega^{(1,3)*}(T_i^*)}{\Omega^{(1,1)*}(T_i^*)}, \tag{6.11}$$

and

$$c^*(T_i^*) = \frac{\Omega^{(1,2)*}(T_i^*)}{\Omega^{(1,1)*}(T_i^*)}. \tag{6.12}$$

A second approximation to the binary diffusion coefficient of a gas is

$$D_{(i,j)_2} = D_{(i,j)_1} \cdot f_{D_{i,j}}^2 \tag{6.13}$$

where

$$D_{(i,j)_1} = 0.002628 \frac{\left[\frac{T^3(M_i + M_j)}{2M_iM_j}\right]^{\frac{1}{2}}}{P\sigma_{i,j}^2 \Omega_{i,j}^{(1,1)*} T_{i,j}^*}. \tag{6.14}$$

The expressions for $\sigma_{i,j}$ and $T^*_{i,j}$ are described by

$$\sigma_{i,j} = \frac{1}{2}(\sigma_i + \sigma_j), \tag{6.15}$$

and

$$T^*_{i,j} = \frac{T}{\left[\frac{\varepsilon}{k_B}\right]_{i,j}} \tag{6.16}$$

where

$$\left[\frac{\varepsilon}{k_B}\right]_{i,j} = \left\{\left[\frac{\varepsilon}{k_B}\right]_i \cdot \left[\frac{\varepsilon}{k_B}\right]_j\right\}^{\frac{1}{2}}. \tag{6.17}$$

$$f^2_{D_{i,j}} = \frac{1}{1 - \Delta_{i,j}} \tag{6.18}$$

where

$$\Delta_{i,j} = W\frac{\left(6c^*\left(T^*_{i,j}\right) - 5\right)^2}{60\left(X_\lambda + Y_\lambda\right)}, \tag{6.19}$$

$$\begin{aligned} W = \; & \frac{X_i^2 M_i}{\lambda_{i_1} M_j} + \frac{X_j^2 M_j}{\lambda_{j_1} M_i} + \\ & \frac{2X_i X_j}{\lambda_{i,j_1}}\left[1 + \frac{15\left(M_i - M_j\right)^2}{8A^* T^*_{i,j} M_i M - j}\right], \end{aligned} \tag{6.20}$$

$$X_\lambda = \frac{X_i^2}{\lambda_{i_1}} + \frac{2X_i X_j}{\lambda_{i,j_1}} + \frac{X_j^2}{\lambda_{j_1}}, \tag{6.21}$$

and

$$Y_\lambda = U^1 \frac{X_i^2}{\lambda_{i_1}} + U^Y \frac{2X_iX_j}{\lambda_{i,j_1}} + U^2 \frac{X_j^2}{\lambda_{j_1}}. \tag{6.22}$$

The expression for U^1, U^2, and U^Y are described by

$$\begin{aligned} U^1 = \; & A^* T^*_{i,j} \frac{4}{15} + \frac{(M_i - M_j)^2}{2M_iM_j} \\ & - \left(\frac{B^* T^*_{ij}}{5} + \frac{1}{12} \right) \frac{M_i}{M_j}, \end{aligned} \tag{6.23}$$

$$\begin{aligned} U^2 = \; & A^* T^*_{i,j} \frac{4}{15} + \frac{(M_j - M_i)^2}{2M_iM_j} \\ & - \left(\frac{B^* T^*_{ij}}{5} + \frac{1}{12} \right) \frac{M_j}{M_i}, \end{aligned} \tag{6.24}$$

and

$$\begin{aligned} U^Y = \; & - \left(\frac{B^*(T^*_{ij})}{5} + 1 \right) \\ & - \frac{\left(12B^*(T^*_{i,j}) - 25\right)(M_i - M_j)^2}{32A^*(T^*_{i,j})M_iM_j} \\ & \frac{A^*(T^*_{i,j})(M_i + M_j)\lambda^2_{i,j_1}}{15M_iM_j\lambda_{i_1}\lambda_{j_1}}. \end{aligned} \tag{6.25}$$

The thermal diffusion ratio in a mixture is

$$k_{i,m} = \sum_{\substack{j=1 \\ j \neq i}}^{nspc} k_{i,j} \tag{6.26}$$

where

$$k_{i,j} = \frac{X_i X_j (M_i - M_j)\left(30A^*(T^*_{i,j}) + 75\right)\left(6c^*(T^*_{i,j}) - 5\right)}{A^*(T^*_{i,j})M_i M_j\left(32A^*(T^*_{i,j}) - 24B^*(T^*_{i,j}) + 110\right)} \tag{6.27}$$

which leads to the thermal diffusion coefficient, $D_{i,T}$.